

IRON OXIDE – GRAPHENE OXIDE NANOCOMPOSITIONS AS ADSORBENTS

A Thesis

presented to the Faculty of the Graduate School

at the University of Missouri-Columbia

In Partial Fulfillment

of the Requirements for the Degree

Master of Science

By

FADI TANTISH

Dr. Maria Fidalgo, Thesis Supervisor

DECEMBER 2016

The undersigned, appointed by the Dean of the Graduate School, have examined the thesis
entitled:

IRON OXIDE – GRAPHENE OXIDE NANOCOMPOSITES AS ADSORBENTS

Presented by Fadi Tantish,

A candidate for the degree of Master of Science,

And hereby certify that, in their opinion, it is worthy of acceptance.

Dr. Maria Fidalgo

Dr. Enos C. Inniss

Dr. Jian Lin

Acknowledgements

To my precious advisor, Dr. Maria Fidalgo, I send my deepest and most sincere appreciation for her continuous guidance, patience, kindness, good humor, enthusiasm, and encouragement all the way through my graduate studies.

To my ultimate treasure in this world, my mom, dad, brothers, and sisters, who kept pushing me forward to earn this degree. Also, many thanks to my uncles and aunts who kept cheering me during my stay in the US, and a special thanks for my uncle Amjed Tantish who supported me from the start to win this golden opportunity.

To Dr. Enos Inniss in the Department of Civil and Environmental Engineering and Dr. Jian Lin in the Department of Mechanical Engineering for sitting on my thesis committee and also for their support and advices.

To my valuable labmates, Max Storms, Mohammed Bayati, Abbas Kadhem, Mohammed Hussain, Mohammed Numaan, Jingjing Dai, Austin Zambrana, and Daryl Rockfield, for their continuous support and kind friendship which helped forming my work. Not forgotten my assistants, Carly Clint, Megane Potthast, InHan Kim for dedicating their time to assist me in my work.

To my sponsor, USAID, for giving me the chance to change my life by earning this master degree. Also, many thanks to my program officers, Amirah Nelson and Jessica Ellerbach, for their priceless support and facilitation.

Finally, to the University of Missouri. For hosting me and for the opportunities she gave me. MIZ-ZOU forever!

Table of Contents

Acknowledgements.....	ii
Table of Figures	vi
Table of Tables	viii
Abstract.....	ix
1 Introduction	1
2 Objectives.....	3
3 Literature Review	4
3.1 Ceramic membranes.....	4
3.2 Ferroxane and ceramic materials.....	5
3.3 Graphene Oxide.....	6
3.4 Arsenic	9
3.4.1 Occurrence.....	9
3.4.2 Toxicity.....	11
3.4.3 Mobility.....	11
3.4.4 Arsenic Removal methods.....	12
3.5 Adsorption processes of arsenic removal.....	15
3.5.1 Surface area.....	17
3.5.2 Effect of pH.....	17
3.5.3 Oxidation state of arsenic.....	18

3.5.4	Competing ions	18
3.5.5	Temperature	18
4	Materials and Methods	19
4.1	Materials synthesis	19
4.1.1	Lepidocrocite synthesis.....	19
4.1.2	Ferroxane Synthesis	20
4.1.3	Graphene Oxide Synthesis.....	20
4.1.4	Composite Material Production	21
4.2	Materials characterization	22
4.2.1	X-Ray Diffraction	22
4.2.2	Surface Charge (Zeta Potential).....	23
4.2.3	Specific Surface Area	24
4.2.4	Size Distribution	25
4.2.5	SEM Imaging.....	27
4.2.6	Adsorption isotherms and kinetics.....	28
4.3	Experimental Methods	29
4.3.1	Membrane Fouling.....	29
4.3.2	Adsorption of arsenic.....	33
4.4	Modeling	35
4.4.1	Adsorption kinetic models	35

4.4.2	Adsorption Isotherms models	36
5	Results and Discussion	38
5.1	Materials characterization	38
5.1.1	Materials Production	38
5.1.2	X-Ray Diffraction	40
5.1.3	Surface Charge	41
5.1.4	Surface Area	44
5.1.5	SEM Imaging	45
5.1.6	Size	52
5.2	Membrane Fouling Characterization	59
5.3	Adsorption of Arsenic	62
5.3.1	Adsorption isotherms of arsenic	62
5.3.2	Adsorption Kinetics	66
5.3.3	Adsorption Mechanism	68
6	Conclusions	70
7	Further works	72
8	References	73
9	Appendix	78

Table of Figures

Figure 3-1: GO chemical structure and the attached functional groups.	7
Figure 3-2: Different types of interactions involved in the adsorption of pollutants on metal oxide/graphene oxide.	8
Figure 3-3: Distribution of arsenate and arsenite ions as a function of pH [44].....	10
Figure 3-4: Basic terms of adsorption.....	15
Figure 4-1: Schematic illustrating experimental set up for lepidocrocite synthesis	20
Figure 4-2: Amicon millipore stirred ultrafiltration cell.....	30
Figure 4-3: Schematic of the membrane fouling experiment [8].....	33
Figure 5-1: Produced materials: (a) Ferroxane, (b) Graphene Oxide (GO), (c) 5% GO/IO and 10% GO/IO composite materials.	38
Figure 5-2: (a) Aggregates after few seconds of mixing both IO and GO, (b) Aggregates during stirring after approximately two minutes of mixing, (c) Settled aggregates after few minutes of stirring.	39
Figure 5-3: X-ray diffractogram for sintered (a) 5% GO/IO composite material, (b) 10% GO/IO composite material.	40
Figure 5-4: Zeta Potential for ferroxane and graphene oxide, suspended in ultra-pure water, as a function of pH.	42
Figure 5-5: Zeta potential for the sintered 5% GO/IO and 10% GO/IO composite materials as a function of pH.	43
Figure 5-6: SEM image for ferroxane nanoparticles.	45
Figure 5-7: TEM image for GO nanoparticles (sheets).	46

Figure 5-8: SEM images for suspended aggregates of (a) 5% GO/IO-A composite, (b) 10% GO/IO-A composite.	47
Figure 5-9: EDS analysis for the 5% GO/IO composite.....	48
Figure 5-10: EDS analysis for the 10% GO/IO composite.....	49
Figure 5-11: SEM images for sintered aggregates of (a) 5% GO/IO composite, (b) 10% GO/IO composite.....	50
Figure 5-12: SEM images for strange holes in the surface of the composites.....	52
Figure 5-13: Z - average and number mean diameters distribution of GO with respect to pH. ..	53
Figure 5-14: Z - average and number mean diameters distribution of IO with respect to pH.....	54
Figure 5-15: SEM images for composite materials (a) 5% GO/IO-A dried at room temperature, (b) 5% GO/IO-A dried inside an oven at 70°C, (c) 10% GO/IO-A dried at room temperature, (10) 5% GO/IO-A dried inside an oven at 70°C.	55
Figure 5-16: Histogram of the diameters' frequency distribution for composite material (a) 5% GO/IO-A, (b) 10% GO/IO-A	57
Figure 5-17: Histogram of the diameters' cumulative distribution for composite material (a) 5% GO/IO-A, (b) 10% GO/IO-A.	57
Figure 5-18: Films created by large aggregates of: (a) 5% GO/IO-A composite, (b) 10% GO/IO-A composite.....	58
Figure 5-19: pure ferroxane coated supports after sintering.....	59
Figure 5-20: (a) 10% GO/IO-A composite layer peeled after drying at room temperature for 24 hours. (b) 5% GO/IO composite layer cracked after sintering. (c) 10% GO/IO composite layer produced by the fifth method.	60

Figure 5-5-21: Adsorption isotherms for arsenic, effect of pH and ionic strength. at (a) IS 1 mM, (b) IS 100 mM, (c) pH 4.5, and (d) pH 7; [As(v)] is between 0.5 and 10 ppm, and [adsorbent] is 400 ppm. 62

Figure 5-22: Non-linear regression models for arsenic removal at arsenic at (a) IS 1 mM, (b) IS 100 mM, (c) pH 4.5, and (d) pH 7; [As(v)] is between 0.5 and 10 ppm, and [adsorbent] is 400 ppm. 65

Figure 5-23: Adsorption kinetic of arsenic removal at pH 7 and IS 100 mM for both composites. 66

Figure 5-5-24: Non-linear pseudo second-order kinetics method and experimental kinetics for arsenic adsorption by both composites at pH 7 and IS 100 mM. 67

Table of Tables

Table 3-1: Principal Reactions Affecting Inorganic Arsenic Concentrations in Ground Water. 12

Table 3-2: Adsorption processes in water treatment..... 17

Table 5-1: 5% GO/IO-A aggregates' size data obtained from SEM. 56

Table 5-2: 10% GO/IO-A aggregates' size data obtained from SEM. 56

Table 5-3: Best fit models with their parameters for different conditions. 64

Abstract

Iron oxides and carbon containing materials are recognized for their potential in the water treatment field as adsorbent materials for removing many contaminations such as heavy metals and organic matter. One of these iron oxides is hematite, which was examined by many researchers during the last few years, and it showed pleasing adsorption capacity. As a carbon containing material, graphene oxide is a rising star in many fields due to its vast properties and its ability to enhance the properties of other materials that are mixed with it. The aim of this work is to investigate the possibility of increasing the adsorption capacity of hematite further by the addition of graphene oxide to form a new composite material. In short, the raw materials for the new composite were synthesized. Lepidocrocite was synthesized from ferrous chloride then acidic acid was added to it to form ferroxane nanoparticles (precursor of hematite) while graphene oxide was synthesized from graphite by applying modified Hummer's method. The following step was characterizing the raw materials (ferroxane and graphene oxide) to look at their properties (size, surface charge, surface area, and morphology) before composing them. The major factor that controlled the composing process was the electrostatic attraction, in order to get fast aggregation instead of growing aggregation, and the chosen pH for composing the raw material was determined to be around pH 4. Two weight ratios were chosen for the new composite materials aggregates, 5% graphene oxide to 95% iron oxide (5% GO/IO-A) and 10% graphene oxide to 90% iron oxide (10% GO/IO-A). For the purpose of fabricating the new composites onto the ceramic membranes, many ways were tried, but none of them formed a stable surface layer on the ceramic membrane. The composites were sintered at 410 °C to form 5% GO/IO and 10% GO/IO composites. Then, the same characterization methods applied to the raw materials were applied to measure the properties of the new composites. Arsenic, As (v),

was chosen to be the adsorbate material in the adsorption experiments. To conduct the adsorption isotherms experiment, different concentrations of arsenic solutions, between 0.5 ppm to 10 ppm, were prepared from sodium arsenate, and the concentration of the adsorbents, composites, in each sample was 400 ppm. The experimental conditions were pH 4.5 and pH 7 with ionic strength of 1 mM one time, and 100 mM in the second time. As for the adsorption kinetics experiment, a solution of 10 ppm of As (v) with ionic strength of 100 mM at pH 7 was prepared and 500 mg of the adsorbents were added to each 1 L of the solution. The results showed a slight decrease in the surface area of the new composites (65.98, 68.05 m²/g for the 5% GO/IO and 10% GO/IO composites, respectively) than the hematite (73.87 m²/g) while the surface area of the graphene oxide was 151.4 m²/g. In addition, the highest adsorption capacity occurred for the 10% GO/IO composite at pH 7 and ionic strength 100 mM (almost 18 mg As(v)/g adsorbent). The kinetics experiments demonstrated that almost 60% of As(v) was adsorbed by both composites after two hours while the saturation occurred after 17 hours with 7.9 mg/g, 8.8 mg/g and for the 5% GO/IO and 10% GO/IO composites, respectively.

1 Introduction

For many centuries, arsenic was acknowledged in many fields, especially in medicine, and science, because of its bad reputation as a poison for life beings. Nowadays, natural arsenic contamination in groundwater is considered to be the worst worldwide problem of water contamination by natural causes [1]. Dangerous and high concentrations of arsenic have been reported during the recent decades from Bangladesh, China, Taiwan, USA, India, Argentina, and many other countries [2]. Among all these countries, Bangladesh is suffering from the highest reported concentrations of arsenic in groundwater, and millions of people over there are high risk for being exposed directly to contaminated water sources [3]. As a response to this global problem, many technologies were introduced to remove arsenic that rely, mainly, on physical-chemical treatment [4].

Under the physical-chemical treatment approach, there are four broad categories [5]: precipitative processes, adsorption processes, ion exchange processes, and membrane (separation) processes. Coagulation/filtration, iron/manganese oxidation, coagulation assisted microfiltration, enhanced coagulation, and lime softening are some precipitative techniques that force arsenic to precipitate by oxidation then the sediments are removed by filtration process. Ion exchange systems can effectively remove As (V), which has a negative charge, but not As (III), which is uncharged [6]. As for membrane processes, arsenic can be removed through several methods such as filtration, electric repulsion, and adsorption of arsenic-bearing compounds [5]. The adsorption process attracts many researchers because many materials display high arsenic sorption capacity like activated carbon, activated alumina, metals, metal oxides, and many other materials [7].

Modern advanced techniques examine the possibility of increasing the adsorption capacity of the metals and metal oxides to remove more contaminants by composing these adsorbents with other well-known adsorbent materials. In recent years, graphene oxide was strongly recognized in the field of water treatment as an adsorbent material and in other fields as an enhancing material [8, 9]. Thus, composite materials consist of both metal oxides and graphene oxide can give a birth of new materials that have vast applications in water treatment. Some examples of these composites are: magnetite/reduced graphene oxide ($\text{Fe}_3\text{O}_4/\text{RGO}$) composites [10], MnO_2/RGO and Ag/RGO composites [11], $\text{Fe}(\text{OH})_3/\text{GO}$ composite [12], TiO_2/GO composites [13-15], and many other metals and metal oxides composites with graphene oxide.

Hematite, one of the metal oxides, gains a great interest as an adsorbent due to its relative low-cost, environmental friendly production and the vast amount available in the nature. It was studied previously to see its capacity as adsorbent for arsenic removal [16] . Composing hematite with graphene oxide can results in improvement in the arsenic removal of hematite.

2 Objectives

The goal of this work is to investigate the possibility of improving the performance of hematite (derived from ferroxane) as adsorbent material to remove arsenic by the addition of graphene oxide. Three main objectives were set up to accomplish the goal of this work: 1) synthesizing the raw materials then the new GO/IO composite material, 2) fabricating new ceramic membranes coated with the new composite material, 3) Measuring the arsenic adsorption capacity of the new composite material.

For the first objective, each ferroxane (precursor of hematite) and graphene oxide will be produced and their properties will be measured like: size, shape, surface area, and surface charge. Then, the new composite material will be produced in two ratios according to the weight of each raw material: 5% GO/IO means 5% of the total weight of the composite is GO and 95% is ferroxane, 10% GO/IO means 10% of the total weight of the composite is GO and 90% is ferroxane. Their properties after sintering will be measured as well as the raw material.

In the second objective, some ceramic membranes will be coated with the two composite material, and other will be coated with pure ferroxane then all will be sintered. The permeability of the uncoated and coated membranes will be measured. Also, a fouling experiment will be conducted to observe any change between the ferroxane coated membranes and the new composites coated ones.

Finally, adsorption isotherms and kinetics experiments will be conducted under different conditions of pH and ionic strength to observe the behavior of the new composites at adsorbing arsenic.

3 Literature Review

3.1 Ceramic membranes

Membrane technology gained the attention of many researchers in the last two decades because of its several applications, including drinking water and wastewater treatments. While the conventional water treatment facilities have a larger footprint and less efficiency in removing small contaminants, membrane technology offer smaller footprint facilities and higher efficiency in removing many small contaminants. Two major types of membranes were studied in the literature and were applied to the practical field: polymeric membranes and ceramic membranes. The efficiency of membranes is generally limited by material properties. Thus, there are some advantages and disadvantages of ceramic membranes over polymeric membranes.

The benefits of ceramic membranes are found in their high mechanical strength and stability, high thermal and chemical resistance, high flux and low fouling, and longer operational life [17]. For such properties, ceramic membranes gained trust in drinking water treatment as they can remove and clean many contaminants from water that are coming from different sources while accumulating fewer organic foulants than polymeric membranes[18]. In the other hand, the potential limitations of using ceramic membranes are the high initial capital cost to establish the facility and install the equipment, and the needed special operational experience to operate and work with these kinds of membranes[19].

The deposition of new chemically active materials such as metal oxides, especially iron oxides, over ceramic membranes opens up new opportunities to enhance their properties and increase their application [20]. Ceramic membranes have been shown to act as adsorbents [21], disinfectants [22], and catalysts [23]. As new improved fabrication methods that reduce costs and environmental impacts of ceramic membranes combined with their properties are introduced,

the attention toward using ceramic materials has increased [24] . Further investigation of new materials is necessary to understand their capabilities and characteristics so that the use of ceramic membranes can be advanced [24].

3.2 Ferroxane and ceramic materials

Chemical compounds that consist of iron and oxygen are called iron oxides. In total, there are sixteen known iron oxides and iron oxyhydroxides that have numerous applications in research and technology [25]. They are used as pigments for paints, as building materials, as chemical sorbents, and as catalysts [26, 27]. Many previous works attempted to incorporate iron oxides into both ceramic and polymeric membranes: coating microfiltration membranes with ferrihydrate nanoparticles [28], layer by layer deposition [29, 30], and sol-gel techniques [31]. Improvement in natural organic matter (NOM) removal by iron oxide-coated membranes was detected by the adsorbing fractions, although long term fouling is a concern [30]. Ferroxane, driven from lepidocrocite (one of these iron oxides), attracted many researchers because of the environmentally friendly way of production and the variety of applications that it can be used for.

The use of iron oxides is desirable because their toxicity is low. However, for many metal oxides, the synthesis produces organic pollutants [32]. The most environmentally toxic stage is the shape forming step because a number of binders and solvents (often chlorinated, such as 1,1,1-trichloroethylene [32]) are potentially toxic. The introduction of ferroxane, a novel iron oxide nanomaterial created by reacting organic acid with lepidocrocite, to ceramic materials has been proven to be an environmentally friendly process [33, 34]. In this process, a dispersion of ferroxane nanoparticles is deposited on a support layer and sintered, sintering is the process of applying high temperature on a powdered material to form a solid one, to form the ceramic's coating layer. The formation of ferroxane derived ceramics only requires the use of acetic acid

and a sintering process—no solvents, plasticizers, or bonding agents are necessary. Moreover, the precursor particles are produced in aqueous media and low to moderate temperatures are required during membrane fabrication—this results in significant improvements over other preparation methods with respect to environmental and economic aspects.

A variety of contaminants in water sources were effectively removed by ferroxane derived ceramic materials. Arsenic removal by these ferroxane-derived ceramic membranes has been incorporated into point-of-use treatment methods [21]. Viruses, as well, were successfully removed from water [35]. The potential catalytic capabilities of the ferroxane derived membranes are especially exciting and offer a wide range of applications. Ferroxane derived ceramic materials, and ferroxane derived ceramic membranes in particular, have proven to be an effective, easy-to-use, and environmentally conscious method for water treatment. More complete investigation on the efficiency and capability of these membranes is necessary; improving fouling behavior of these membranes will allow them to be more effective and efficient moving forward.

3.3 Graphene Oxide

Graphene oxide (GO) is a main successor to graphene, a one-atom thick, two-dimensional nanomaterial made of sp²-hybridized carbon that has received extraordinary attention as a result of its properties and wide applications [36].

A variety of functional groups, such as hydroxyl, carboxyl, and epoxy groups, shown in Figure 3-1, were found to be attached to GO, which make GO strongly hydrophilic and permits it to be a good candidate for the retention and pre-concentration of metals, biomolecules, fluorescent molecules, drugs, and inorganic nanoparticles. These properties and its very high theoretical specific surface area make GO an excellent platform for loading magnetic

nanoparticles. The addition of magnetic properties into GO can combine the high sorption capacity of GO and the separation convenience of magnetic materials [37].

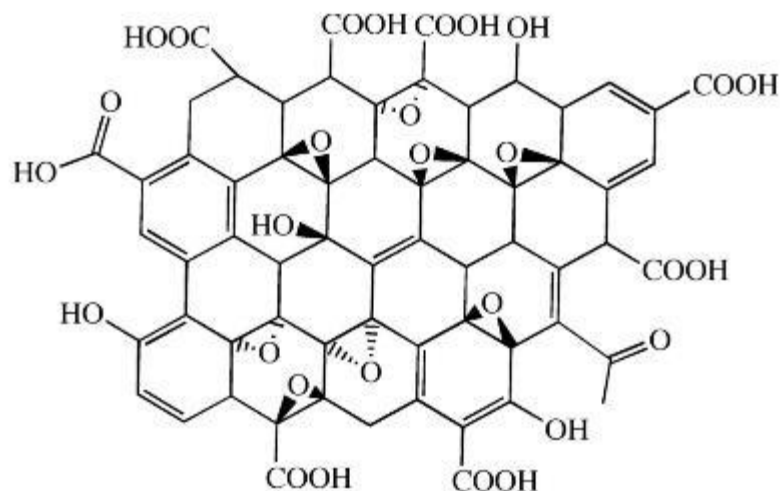


Figure 3-1: GO chemical structure and the attached functional groups.

The large surface area and the high surface hydrophilicity of GO enable strong adsorption affinity and capacity for hydrophobic organic contaminants, and their tunable surface properties at the nano-scale allow optimal binding efficiency and selectivity of the target compounds, making them superior adsorbents. Moreover, the GO surface has some interaction regions which account for the high adsorption affinity. These regions are π - π electron donor-acceptor (EDA) interactions between π - electron-donor compounds (e.g., polycyclic aromatic hydrocarbons and amino- and hydroxyl-substituted aromatics) or π - electron-acceptor compounds (e.g., nitro-aromatics and sulfonamide and tetracycline antibiotics) and the respective polarized π - electron-depleted or π - electron-rich regions. [38].

Combining GO with Fe_3O_4 results in $\text{GO}/\text{Fe}_3\text{O}_4$ material which can be used as an effective sorbent for the simple and rapid removal of inorganic pollutants, metals like Cu(II) , and organic pollutants, like fulvic acid, from water samples. Chemical functionality plays the major role in removing these pollutants [37], see Figure 3-2 for more illustration.

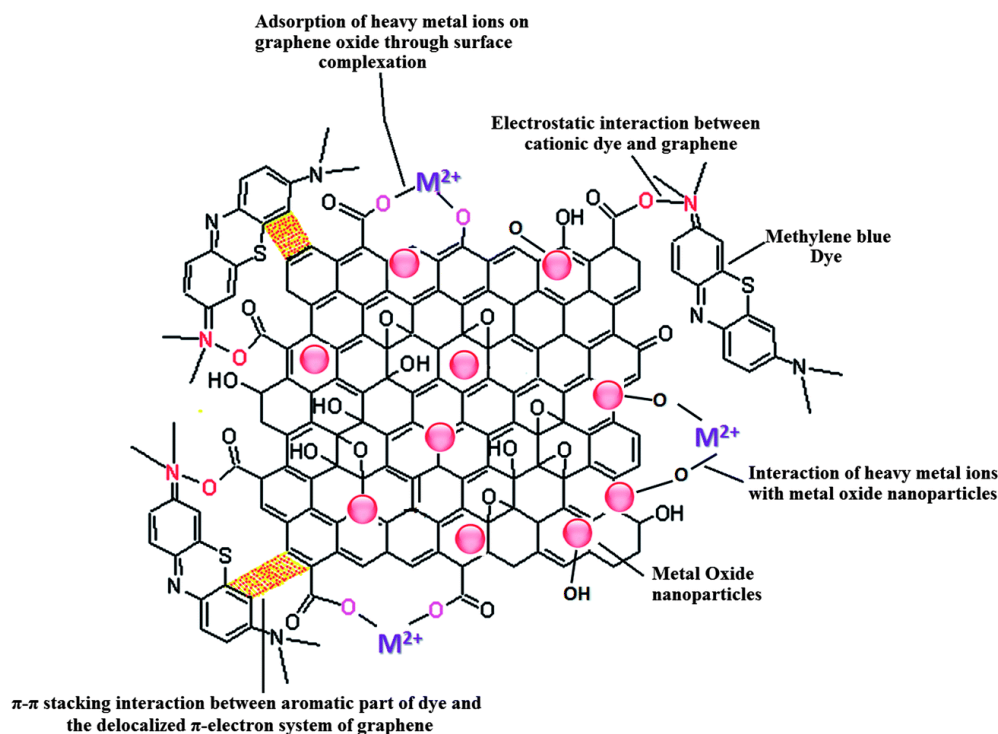


Figure 3-2: Different types of interactions involved in the adsorption of pollutants on metal oxide/graphene oxide.

It has been shown experimentally by L Ji and W Chen that GO can effectively adsorb naphthalene, naphthol, naphthylamine, and tylosin, attributed to specific electron donor–acceptor interaction with the graphitic surfaces and/or Lewis acid–base interaction with the O-functionalities of adsorbents [38].

On the other hand, the negative effect of GO is its potential toxicity to living beings. The amount of toxicity depends on a functional group’s density, size, and conductivity on GO [39]. After much research about toxicological aspects of GO, results showed some toxicity of GO in soil and water environments. In the soil environment, GO is toxic to some crops like cabbage, tomato, red spinach, and lettuce. It is also toxic to *Arabidopsis thaliana* cells suspensions, as well as, having enzyme-dependent toxicity to *Vicia faba* (faba bean). As for water environment, GO is toxic to *Amphibalanus Amphitrite* crustaceans, and to wastewater microbiological communities. Also it has moderate toxicity to zebrafish embryos [40].

No official toxicity mechanisms of GO were reported, but some research proposed some possible mechanisms. Firstly, the oxidative stress of GO was reported to be one of the mechanisms which is involved in the toxic effects of carbon nanomaterials. The generation of reactive oxygen species (ROS) is the reason behind the occurrence of oxidative stress in target cells. Antioxidant enzymes, such as superoxide dismutase or glutathione peroxidase, are able to reduce and eliminate ROS. If homeostasis is not achieved, cellular macromolecules, such as proteins, DNA, and lipids, can be damaged. Secondly, the physical interaction with the sharp edges of GO can damage the cell membrane. Moreover, because of its hydrophobic surface, graphene can significantly interact with cell membrane lipids, causing toxicity [39].

3.4 Arsenic

Arsenic, often referred to as the king of poisons [41], is a common trace element that occurs in the earth's crust and is widely spread all over the environment. It is known for the high toxicity in its inorganic form. The presence of arsenic in ground water is one of the main environmental causes of cancer mortality in the world [1]. Tens of millions of people are exposed to contaminated water sources by arsenic daily around the world: Bangladesh, Taiwan, India, Thailand, Ghana, the US, and other countries [2]. As a result, it is important to study the occurrence, toxicity, mobility, and methods to remove arsenic from water sources.

3.4.1 Occurrence

In the environment, arsenic can be found in different organic and inorganic forms, but in water it is mostly found as the inorganic forms, arsenite As(+3) and arsenate As(+5). In oxic waters, arsenate ($H_nAsO_4^{n-3}$) is generally the dominant form [42]. As for the organic forms of arsenic that occur in groundwater, they are negligible unless affected by industrial pollution [43].

Figure 3-3 shows different forms of arsenate and arsenite ions related to different pH conditions.

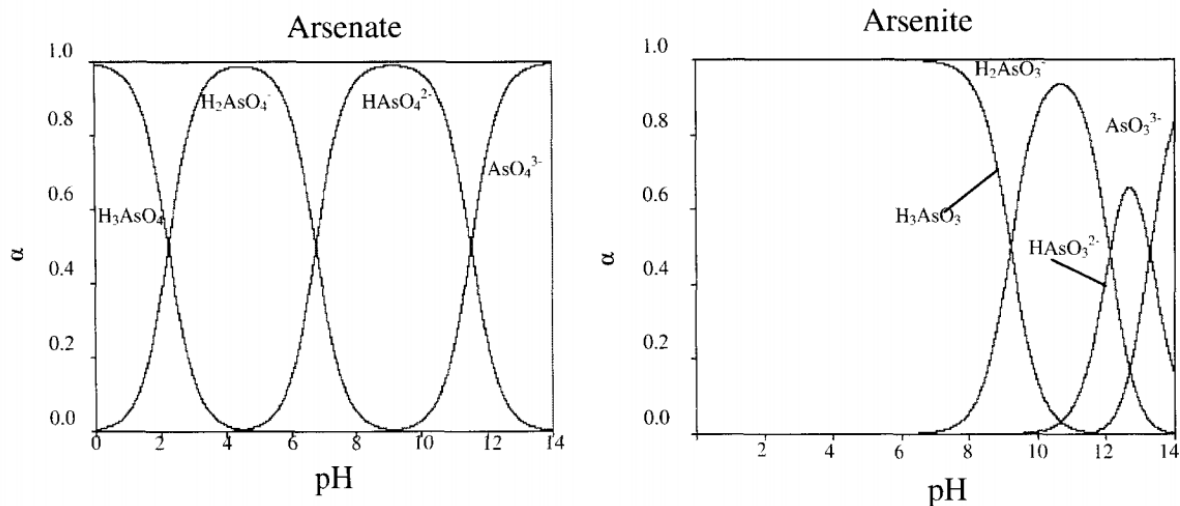


Figure 3-3: Distribution of arsenate and arsenite ions as a function of pH [44].

More than 320 minerals containing arsenic were stated by Fleischer [45], arsenopyrite (FeAsS), orpiment (As_2S_3), realgar (As_2S_2), and solid solution in pyrite (FeS_2) are the most common ones [46]. It was reported that arsenic, in nature, is commonly found in both volcanic and sedimentary rocks adsorbed by Fe(III) and Mn(IV) after weathering of sulfide minerals [47]. Moreover, it can occur due to some anthropogenic sources like chemical disposal from industrial activities, and some pesticides used in agriculture [47].

In the United States, drinking water wells contaminated by different levels of arsenic were discovered in many states like California, Texas, Minnesota, and New England [1]. Some of these wells contain arsenic concentrations higher than $50 \mu\text{g/L}$ [1]. Because of the rising health concerns about the effects of arsenic on the public health, the United State Environment Protection Agency (EPA) adopted to lower the standard for arsenic in drinking water, from $50 \mu\text{g/L}$ to $10 \mu\text{g/L}$, in 2001, to protect consumers from the long-term chronic exposure to arsenic in drinking water [48].

The contamination of ground water by arsenic in Bangladesh is the worst case in the world with millions of people, between 35 million and 77 million, are continually exposed to highly arsenic contaminated drinking water, up to 500 µg/L [3].

3.4.2 Toxicity

Many types of cancer, bladder, skin, and other internal organs, were reported as a result to long-term exposure to low concentrations of arsenic [49]. According to *WHO Fact sheet No 210: Arsenic in Drinking Water - February 1999*, symptoms like hyperpigmentation, depigmentation, keratosis, and peripheral vascular disorders are the most commonly reported for long-lasting arsenic exposure. Skin cancer and a number of internal cancers can also result. Cardiovascular and neurological diseases have also been found to be linked to arsenic digestion and exposure [50].

The toxicity of arsenic strongly depends on the form in which arsenic is present. Inorganic arsenic forms, typical in drinking water, are much more toxic than organic ones that are present in sea food, and the most toxic one among these inorganic forms is As(III) [4].

The lack of feasible treatment approaches for the arsenic problem has resulted in an exceptional interest from the scientific communities, governmental organizations in affected countries, and the profitable sectors of the water segment, as well as from international donors and NGOs and from agencies such as the World Health Organization (WHO) and UNICEF. On the other hand, despite vast provided efforts and funds to find solutions, millions of individuals are still exposed daily to arsenic in their drinking water all over the world [4, 51].

3.4.3 Mobility

Arsenic is a redox-sensitive element, meaning that it can change its form through reduction (gaining an electron) or oxidation (losing an electron) [4]. Thus, its occurrence, mobility, and forms are affected by many geochemical factors, such as pH, reduction-oxidation

reactions, distribution of other ionic species, aquatic chemistry and microbial activity [1]. Table 3-1 [1] illustrates some reactions that affect the concentration of inorganic arsenic concentrations in ground water.

Table 3-1: Principal Reactions Affecting Inorganic Arsenic Concentrations in Ground Water.

Condition	Important Phases	Important Reactions	Conditions That Affect Arsenic Mobility
Oxic (dissolved oxygen present)	Fe-oxides	Adsorption/ desorption	pH; presence of competing adsorbent; oxygen and Fe ³⁺ concentrations
	Sulfide minerals	Precipitation Sulfide oxidation	pH and microbial activity; oxygen and NO ₃ transport
Post-oxic (dissolved oxygen and sulfide not present)	Fe-oxides	Adsorption/ desorption and precipitation Adsorption/ desorption Dissolution	Oxidation state of As pH Presence of organic carbon
	Sulfide minerals	See Oxic discussion above	
Sulfidic (sulfide present)	Sulfide minerals	Precipitation	Sulfide, iron, and As concentrations

In sum, the most common cause of regionally high arsenic concentrations is the release of arsenic from iron oxide, from desorption or dissolution. Desorption can be endorsed by increasing pH to high levels or the introducing a competing adsorbent in oxic and post-oxic ground water [1].

3.4.4 Arsenic Removal methods

Because of its high toxicity and the worldwide investment in searching for removal methods, several treatment technologies were introduced to remove arsenic from drinking water. Some of them were conducted under laboratory conditions while others were conducted under field conditions. Three major technologies were put to work: conventional, physical-chemical, and biological technologies. Generally speaking, the main approach that all technologies rely on for removing arsenic from drinking water is physical-chemical treatment [4]. Under this general approach, there are four broad categories [5]: precipitative processes, adsorption processes, ion exchange processes, and membrane (separation) processes.

All these technologies depend on a few basic chemical processes, which are summarized below [52]:

- **Oxidation/reduction:** reducing or oxidizing chemicals results in altering their chemical form. Such reactions do not remove arsenic from solutions, but are usually used to optimize other processes.
- **Precipitation:** by adding some coagulants to the water, dissolved arsenic can form a low-solubility solid mineral, such as calcium arsenate. This solid can then be removed through sedimentation and filtration.
- **Adsorption and ion exchange:** various solid materials, including iron and aluminum hydroxide flocs, have a strong affinity for dissolved arsenic. Arsenic is strongly attracted to sorption sites on the surfaces of these solids, and is effectively removed from the solution.
- **Solid/liquid separation:** precipitation, co-precipitation, adsorption, and ion exchange all transfer the contaminant from the dissolved to a solid phase. After these processes, either large particles (precipitable), or fine particles (suspended) need to be removed from water using some solid/liquid separation methods, generally sand filters or membranes.
- **Physical exclusion:** some artificial membranes are permeable to specific dissolved compounds and reject others. These membranes can act as a molecular filter to remove dissolved arsenic, along with many other dissolved and particulate compounds.
- **Biological removal processes:** bacteria can play an important role in catalyzing many of the above processes. Relatively little is known about the potential for biological removal of arsenic from water.

Precipitative processes include many techniques [5]: coagulation/filtration, iron/manganese oxidation, coagulation assisted microfiltration, enhanced coagulation, and lime

softening. The precipitate formed after coagulation or in situ oxidation of arsenic with either iron or manganese present in water could be removed by sedimentation followed by rapid sand filtration or of membrane filtration (microfiltration, nanofiltration, or RO) [53]. Coagulation with iron, aluminum salts, and lime softening has been considered the most effective treatment process for removing arsenic from water to meet the primary drinking water regulations standard [4].

Unlike As(III) (uncharged ion in water with a $\text{pH} < 9$), the negatively charged ion As(V) (H_2AsO_4^- , and HAsO_4^{2-}) can be removed by ion exchange systems [6]. Ion exchange systems are widely used in small-scale and point-of-entry systems, treating water as it enters the building, because it is easier to handle and is a sludge-free operation [4]. However, the cost of the treatment is higher than other conventional ones in large-scale systems [5]. In case that As(III) is present in the influent water, it is necessary to oxidize it to As(V) before entering the ion exchange system.

As for membrane processes, arsenic can be removed through several methods such as filtration, electric repulsion, and adsorption of arsenic-bearing compounds. The capability of microfiltration and ultrafiltration as an arsenic removal technique depends on the size distribution of arsenic-bearing particles in water [5]. Significant portions of the dissolved arsenic compounds in natural waters can be removed by nano-filtration membranes. Reverse Osmosis (RO) is a technology proven through several bench- and pilot-scale studies, and is very effective in removing dissolved constituents. Since arsenic in groundwater is typically 80- 90% dissolved, RO is a suitable technology for arsenic removal in groundwater [4].

A variety of untreated water pollutants and characteristics, such as pH value and pollutants size, plays a major role in the effectiveness of membrane filtration for arsenic removal

[54]. It also produces a larger volume of unwanted water contaminated with high arsenic concentrations, and is more expensive than other arsenic treatment technologies. It is therefore used less often than precipitation/co-precipitation, adsorption, and ion exchange [5].

3.5 Adsorption processes of arsenic removal

Adsorption, in general, is a phase transfer process that is widely used in practice to remove undesirable substances from liquids as well as gases. It can be described as an enrichment of chemical species from a fluid phase on the surface of a liquid or a solid [55]. Adsorption has been proven as a fast and inexpensive removal process for a variety of solutes in water treatment [56]. Solute molecules or ions are removed from the aqueous solution by adsorption onto solid surfaces.

The basic terms of adsorption theory are shown in Figure 3-3 [55]. Adsorbent is the solid material that provides the surface for adsorption; the species that will be adsorbed are named adsorbate. A reverse process can occur when the properties of the liquid phase (e.g. concentration, temperature, pH) change. The adsorbed species released from the surface and transferred back into the liquid phase in a process called desorption.

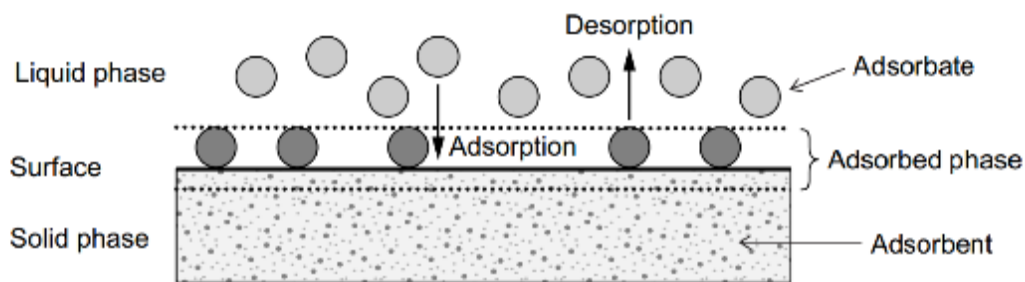


Figure 3-4: Basic terms of adsorption

In general, the adsorption process occurs as a result from either a solute hydrophobicity, or a high affinity of the solute to the adsorbent. Most adsorption processes in waste treatment combine both of them. The solubility of a substance in water is significant. The more hydrophilic

a substance, the less likely it is to be adsorbed. On the contrary, a hydrophobic substance is more likely to be adsorbed. In the context of solute affinity for the solid, it is common to distinguish between three types of adsorption. The affinity may be predominantly due to: (1) electrical attraction of the solute to the adsorbent (exchange adsorption), (2) van der Waals attraction (physical or ideal adsorption), or (3) chemical reaction (chemisorption or chemical adsorption) [57].

Solutes are removed from a solution with a higher concentration at the surfaces of adsorbents, until the amount of solute remaining in the solution is in equilibrium with that at the surface. This equilibrium is described by expressing the amount of solute adsorbed per unit weight of adsorbent, q_e , as a function of the concentration of solute remaining in solution, C_e . An expression of this type is termed as adsorption isotherm. Many equations describe this, but two in particular, the Langmuir equation and the Freundlich equation, are commonly used for describing adsorption isotherms for water and wastewater treatment [57]. These equations will be discussed later in the Modeling section.

Adsorption processes are broadly used in water treatment. Many organic substances as well as inorganic ions can be removed from the aqueous phase depending on the type of adsorbent applied. An overview of typical application fields and treatment objectives are shown in Table 3-2 [55].

Table 3-2: Adsorption processes in water treatment.

Application field	Objective	Adsorbent
water treatment	Removal of dissolved organic matter	Activated carbon
	Removal of organic micropollutants	Activated carbon
Urban wastewater treatment	Removal of arsenic	Aluminum oxide, iron hydroxide
	Removal of phosphate	Aluminum oxide, iron hydroxide
Industrial wastewater treatment	Removal of micropollutants	Activated carbon
	Removal or recycling of specific chemicals	Activated carbon, polymeric adsorbents
Swimming-pool water treatment	Removal of organic substances	Activated carbon
Groundwater remediation	Removal of organic substances	Activated carbon
Treatment of landfill leachate	Removal of organic substances	Activated carbon
Aquarium water treatment	Removal of organic substances	Activated carbon

There are many important factors that control the effectiveness of adsorption processes as a water treatment technique used for the removal of contaminants in general, and arsenic in particular.

3.5.1 Surface area

Surface area of the adsorbent plays a major role in the adsorption process. The larger the specific surface area, that portion of the total surface available for adsorption, the more adsorption of solutes by the adsorbent.

3.5.2 Effect of pH

pH might have a significant effect on removing contaminants by the majority of methods of removal used in water treatment. It determines the point of zero charge, and what is the oxidation status of the ions in water as well as for the adsorbents. Arsenic, for example, has a point of zero charge at pH 8.2. If the pH is below this point, the predominant arsenic species is arsenate, and if the adsorbent has a positive charge below this point, its preference for adsorption is arsenic anions. Low pH levels, an acidic environment, are generally considered optimum for arsenic removal [5].

3.5.3 Oxidation state of arsenic

Like most treatment technologies, the oxidation state of arsenic, or other contaminants, plays a big role in the removal process. As discussed before, some technologies, like ion exchange, work very well in removing arsenate As(V), which is negatively charged. To remove arsenite As(III), which is uncharged, it must be oxidized to arsenate. For instance, if the adsorbent tends to have a positive surface charge, it will attract more arsenate ions than arsenite ions due to the electrical attraction forces.

3.5.4 Competing ions

It is important to know the preference of the adsorbent towards specific ions. For example, activated aluminum preferentially adsorbs arsenate over arsenite [5].

3.5.5 Temperature

Adsorption reactions are normally exothermic, thus decreasing temperature results in increasing the adsorption. Changes in enthalpy for adsorption are usually of the order of those for condensation or crystallization reactions. Therefore, the adsorption process will scientifically change by the small variations in temperature [57].

In conclusion, the efficiency of adsorption processes for arsenic removal are affected by characteristics and contaminants other than arsenic more than precipitation processes. Small scale systems using these technologies tend to have lower operating and maintenance costs and require less operator expertise. Adsorption, therefore, tends to be used more often when arsenic is the only contaminant to be treated for relatively smaller systems [4].

4 Materials and Methods

4.1 Materials synthesis

The first step in this work was to prepare the raw materials, Ferroxane and Graphene Oxide, that will form the new composite material.

4.1.1 *Lepidocrocite synthesis*

In order to synthesize ferroxane nanoparticles, lepidocrocite (γ -FeOOH) was synthesized first from ferrous chloride (**Error! Reference source not found.**). It was synthesized through the oxidation of FeCl₂ under controlled pH conditions, according to published methods [27]. A 0.2M solution of iron(II) chloride tetrahydrate (99% Sigma, St. Louis, MO, USA) in ultrapure water (18m Ω) was prepared. Air was provided throughout the reaction by a diffuser, and pH was monitored. The pH was initially 2.6, so 1M NaOH (Acros, NJ, USA) was added until the pH reached approximately 6.5, roughly 40mL. Throughout the reaction, pH was maintained between 6.7 and 6.9 by addition of 0.1M NaOH, with continuous agitation and aeration for approximately 3 hours, until an orange precipitate was obtained. The precipitate was centrifuged for 8 minutes at 3,500rpm and the supernatant was discarded. The product was then purified: the precipitate was re-suspended and centrifuged 3 additional times to remove NaCl produced during the oxidation. The precipitate was finally dried at 50°C in a crystallization dish to yield the final product. This process generally produced roughly a 50% yield [27].

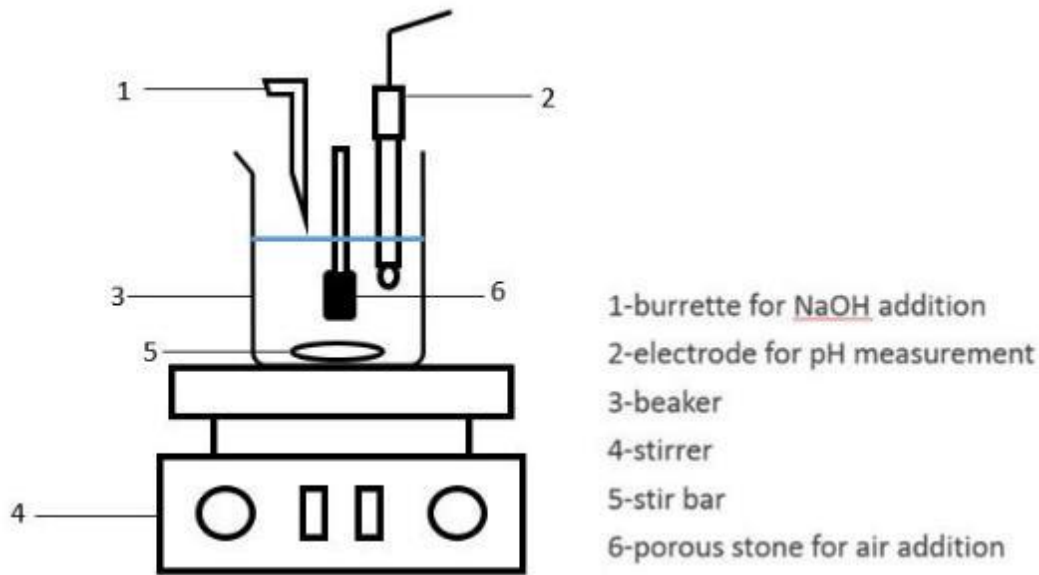


Figure 4-1: Schematic illustrating experimental set up for lepidocrocite synthesis

4.1.2 *Ferroxane Synthesis*

Ferroxane nanoparticles were prepared by reaction lepidocrocite particles with acetic acid [58]. In short, lepidocrocite particles were suspended in ultrapure water (18m Ω) followed by addition of glacial acetic acid (Fisher, Nazareth, PA, USA) to give a molar ratio of 2:1 (acetic acid to iron). The reaction was allowed to continue for 3 hours while stirring the solution at 600 rpm at 70°C, with a reflux condenser in place to keep the acetic acid concentration constant. Finally, the suspension was centrifuged for 8 minutes at 3,700rpm to remove unreacted lepidocrocite particles. The supernatant was collected and placed in the oven at 50°C to dry.

4.1.3 *Graphene Oxide Synthesis*

Modified Hummer's method was used to synthesize GO from Graphite nanoplatelet (5 μ m, xGnP graphite nanoplatelet XG Sciences) [59]. In brief, 1 g of graphite and 1 g of NaNO₃ (Sigma-Aldrich) were mixed together in an ice-bath followed by adding 46 ml of 98% (w/w) H₂SO₄ (Fisher Scientific). Then, 6 g of KMnO₄ (Flinn Scientific) was carefully added into

the mixture. After stirring for 1 h at 35 °C, 80 mL of ultrapure water (18 MΩ.cm) was added carefully to the mixture and the temperature was increased to 90°C for 30 min. Then, 200 ml of ultrapure water with 6 ml of 30% H₂O₂ (Fisher Scientific) were added to the reaction system. The resulting mixture was washed with DI water at least 30 times to obtain pH 5. Finally, the final GO was obtained using exfoliation under ultrasonication for 45 min in a Branson 2510 ultrasonic bath at a frequency of 42 kHz.

4.1.4 Composite Material Production

According to the literature [60, 61], IO shows a change in surface charge from a positive charge at pH less than 8 to a negative charge at pH greater than 8. On the other hand, GO shows a negative charge at all pH values. In light of these characteristics, the concept of Electrostatic Attraction between both ferroxane and GO can be applied to form the new composite material. Thus, the best condition to create the composite material occurs when pH values of both solutions, IO and GO, are acidic.

By applying this concept in this work, two different composite materials were created from IO and GO. The first one is 5% GO/IO-A composite material in which 5% of the total weight is GO, and 95% is ferroxane. Both of them were separately re-suspended in ultrapure water (18 MΩ.cm) then they were mixed together at pH 4. The second one is 10% GO/IO-A composite material in which 10% of the total weight is GO, and 90% is ferroxane. Also, both of them were separately re-suspended in ultrapure water (18 MΩ.cm) then they were mixed together at pH 4. For example, to prepare a sample composite material of 1000 ppm, 950 mg of ferroxane and 50 mg of GO need to be mixed together to form the 5% composite material while 900 mg of ferroxane and 100 mg of GO need to be mixed together to form the 10% GO/IO-A composite material. Than total mixing time was 6 hours. Then, the produced composite materials were dried in an oven at 80 °C. The last step is the sintering process at which composite

materials kept in a furnace (Vulcan 3-550, Neytech, USA) then the temperature was gradually increased as following: 1) temperature was raised to 100 °C with a constant rate of 1°C/min and kept on hold for 2 hours. 2) temperature was raised again to 280 °C with a constant rate of 1°C/min and kept on hold for 3 hours. 3) finally, temperature was raised to 410 °C with a constant rate of 1°C/min and kept on hold for 4 hours. The outcome composites were 5% GO/IO, and 10% GO/IO.

4.2 Materials characterization

To understand the structure and properties of IO and GO, and the composite materials, several characterization techniques were used, such as x-ray diffraction, surface charge, surface area, size distribution, and scanning electron microscopy (SEM).

4.2.1 X-Ray Diffraction

(Ultima IV X-Ray Diffractometer—Rigaku, Japan)

X-ray powder diffraction (XRD) is a quick analytical technique mainly used to identify the phase of a crystalline material and can provides information on unit cell dimensions. The material should be grounded very well and homogenized to start the analysis, and average bulk composition is determined [62].

XRD is based on the scattering of the x-rays after hitting the structure's surface as well as the constructive interference of the waves that are in phase. Based on the scattering and the dispersion in space, the crystalline structure will display a certain signature that is unique.

Bragg's law describes this phenomenon and can predict the direction in which constructive interference occurs between the X-ray beams scattered by the crystalline structure.

$$n\lambda = 2d \sin\theta \quad (\text{Equation 4.1})$$

where n is the order of diffraction, λ is the wave length of the x-ray beam, d is the inter-planar distance, and 2θ is the angle of diffraction [63].

It is a very effective method of identification in the process of material synthesis because it can confirm or deny that the actual product is the desired product, since the resultant diffractogram from X-ray diffraction is like a digital signature for a crystalline structure. The analyzed materials' diffractograms are compared with the existing, published ones, and the comparison results will confirm or deny what kind of material was obtained.

4.2.2 Surface Charge (Zeta Potential)

(Zetasizer Nano ZS ZEN3600—Malvern, UK)

Zeta Potential analysis is a method that defines the surface charge of nanoparticles suspended in liquid media. Generally, most nanoparticles have a surface charge that attracts opposite charged ions to the nanoparticle surface, resulting in forming a tiny layer around the nanoparticles. This layer of ions travels with each nanoparticle as it diffuses throughout the solution. A stable entity is formed between the ions and particles by a notional boundary within the diffused layer. Ions within this boundary move with the particle as it moves, but any ions beyond the boundary do not travel with the particle. This boundary is called the surface of hydrodynamic shear or slipping plane. The electric potential at this boundary is known as the Zeta potential of the particles, and has values that typically range from +100 mV to -100 mV. The magnitude of the zeta potential is predictive of the colloidal stability. Nanoparticles with Zeta Potential values greater than +30 mV or less than -30 mV typically have high degrees of stability. Dispersions with a low zeta potential value will eventually aggregate due to Van Der Waal inter-particle attractions [64].

pH is playing a major role in the determination of zeta potential. A zeta potential value is a meaningless number on its own if pH was not mentioned with it [64]. pH of a solution can affect surface charge because the functional groups attached to the surface of particles, such as hydroxyl and carboxyl, can be protonated or deprotonated to become charged as pH changes.

Thus, as pH increases or decreases, the surface charge of the particles will change. When the total positive charge and total negative charge equals to each other at a certain pH, the net charge of the particle will be zero and this called point of zero charge (pzc).

The Zetasizer Nano series calculates the zeta potential by determining the Electrophoretic Mobility followed by applying the Henry equation (Equation 4.2).

$$U_E = \frac{2 \varepsilon z f(ka)}{3\eta} \quad (\text{Equation 4.2})$$

Where z is zeta potential, U_E is the electrophoretic mobility, ε is dielectric constant, η is the viscosity, and $f(ka)$ is Henry's function which usually is either 1.5 or 1 [65].

The electrophoretic mobility is obtained by performing an electrophoresis experiment on the sample and measuring the velocity of the particles using Laser Doppler Velocimetry (LDV) [64].

A small amount (less than 10mg) of ferroxane was suspended in 100mL of ultrapure water (18m Ω). Then, 1 mL of the ferroxane solution was put into a plastic cuvette for analysis. Similarly, the same weight and volume was used for GO analyses, but a sonication device was used to re-suspend GO in the ultrapure water.

4.2.3 Specific Surface Area

(Coulter SA3100—Beckman Coulter, USA)

One of the well-known methods in analyzing surface area of a solid's powder is Brunauer, Emmett, and Teller (BET) which is based on the adsorption of a gas by a solid, and it reveals valuable information about the specific surface area and pore size distribution of the solid. The most commonly used gas as an adsorbate is nitrogen at its boiling point (77K). By the BET method, the specific surface area of the material is determined based on the Langmuir model—essentially, a known amount of gas is used to form a monolayer of gas molecules on a

solid, and the occupied area of these adsorbed molecules makes it possible to estimate the area of the solid [66].

In this work, 0.25 g of each composite material was weighted and put inside an empty sample cell. Before the specific surface area of the sample can be determined, it is necessary to remove gases and vapors that may have become physically adsorbed onto the surface after the syntheses and during handling and storage. This process called outgassing, and generally involves heating the samples for a period of time in a flow of helium or nitrogen. If outgassing is not achieved, the specific surface area may be reduced or may be variable because part of the surface area is covered with molecules of the previously adsorbed gases or vapors. The outgassing conditions, temperature, pressure and time, are critical for obtaining precise and accurate results for specific surface area measurements.

After finishing the outgassing process, the cell was removed and sealed directly by a rubber stopper. The stopper was removed at the time of weighting the sample after the outgassing. The cell was attached to the volumetric apparatus, and it was submerged in a Dewar vessel containing liquid nitrogen at 77.4 K.

The same happened for the pure hematite with a sample weight of 0.2 g.

4.2.4 Size Distribution

In this work, two methods were used to characterize the sizes of the different materials obtained during the research. One of them is Dynamic Light Scattering which used to determine the size distribution profile of both ferroxane and GO with respect to pH values. The second one is Scanning Electron Microscopy which used to obtain the size distribution of the composite materials.

4.2.4.1 Dynamic Light Scattering

(Zetasizer Nano ZS ZEN3600—Malvern, UK)

Measuring the random changes in the intensity of light scattered from a suspension or solution can determine the particle size in this suspension. A monochromatic light source is shot into a sample, the light is scattered by the particles, and the scattered light is then collected by a photomultiplier. With a narrow-beam laser light and a small scattering volume, the resultant intensity that can be observed is the vectorial sum of the scattering from each of the particles in the suspension. The observed intensity is dependent upon the type of interference, constructive or destructive. Small particles in suspension undergo random thermal motion known as Brownian motion, so their positions are changing which result in fluctuating scattering intensity over time. These fluctuations are correlated, and an auto-correlation function for the intensity of scattered light can quantify this correlation [67]:

$$G(\tau) = [I_s(t)I_s(t+\tau)] \quad \text{(Equation 4.3)}$$

where I_s is the scattering intensity, t is time, and τ is the time shift. The usefulness of $G(\tau)$ is that it can be directly related to the particle diffusivity for a dispersion of monodisperse particles [67]:

$$G(\tau) = A_0 + Ae^{-\Gamma\tau} \quad \text{(Equation 4.4)}$$

$$\Gamma = Q^2D \quad \text{(Equation 4.5)}$$

where A_0 is the background signal, A is an instrument constant, and Γ is the decay constant. The measured decay constant gives the particle diffusion coefficient, according to the equation [67]:

where Q is the magnitude of the scattering wave vector, and D is the particle diffusion coefficient. When the particle diffusion coefficient is found, particle radius can be found, assuming spherical shape [67]:

$$a = \frac{kT}{6\pi\mu D} \quad (\text{Equation 4.6})$$

where a is particle radius, k is the Boltzmann constant, and T is temperature.

A small amount (less than 10mg) of ferroxane was suspended in 100mL of ultrapure water (18m Ω). Then, 1 mL of the ferroxane solution was put into a plastic cuvette for analysis. Similarly, the same weight and volume was used for GO analyses, but a sonication device was used to re-suspend GO in the ultrapure water.

4.2.4.2 SEM sizing

(Quanta 650 FEG—FEI, USA)

Scanning Electron Microscopy (SEM) uses a high energy electron beam and scan over the surface and the back scattering of the electrons is looked at. The sample must be under a vacuum and must be conductive. This requirement can be restrictive and this technique can be time consuming and expensive. More details about SEM in the coming section.

In this work, four samples were prepared (two 5% GO/IO-A and two 10% GO/IO-A), two inside the lab and were dried using room temperature while the other two were prepared in SEM department and were dried using the oven. Each one of them was scanned by SEM, and the mean diameter was measured from the photos.

4.2.5 SEM Imaging

(Quanta 650 FEG—FEI, USA)

SEM is a characterization technique used to observe and image small-scale materials. It uses electrons rather than light to generate images—this makes the resolution of SEM controlled by the wavelength of electrons rather than by the wavelength of light. At the standard energy of 5keV, this wavelength is only 0.55 nm [68]. Adding other limiting factors, such as lens aberration, the ultimate resolution of a 5keV SEM is on the order of a few nanometers [68], making it ideal for imaging the nanomaterials used in this work.

As discussed before, SEM uses a high energy electron beam and scan over the surface of the material along a path of parallel lines and the back scattering of the electrons is looked at. The signals produced by the electrons and radiation that result from the impact are collected by a detector and amplified [68]. The result is an enlarged topographic image of the sample.

SEM produces high-resolution images (10 to 100,000 times magnification), and requires that samples are conductive [68]. In some cases, it can take images of non-conductive samples at low voltage. SEM is a widely used method for studying the topography of solid materials, organic and inorganic. In this work, SEM was used to view what kind of aggregation will occur after mixing both IO and GO in different ratios.

In order to obtain images, silica layers were choosing to work as a background, and they were fixed on metal supports by using carbon tape. Samples of both suspended composite materials, not sintered, were added as drops on the silica layers, and were dried in the oven. Another samples of dry sintered composite materials were directly attached to the carbon tape, without using the silica layers, because the composite materials were magnetic, and can cause a damage to the machine.

4.2.6 Adsorption isotherms and kinetics.

(Atomic Absorption Spectrophotometer, Buck Scientific – 210 VGP)

Adsorption process is described usually through graphs called isotherms which show the amount of adsorbate adsorbed on the surface of adsorbent in aqueous solutions as a function of its concentration at constant temperature. There are about 15 different isotherms models were developed up until now [69]. In order to be able to work with these models, experimental data must be available.

It has been discussed before the concept of adsorption process and the factors affecting it. More about some models and equations used in describing the adsorptions isotherms and kinetics are located in **section 4.4**.

In this work, all the collected samples during the adsorption experiments were firstly diluted to 100 ppb then they were tested using Atomic Absorption Spectrophotometer with graphite furnace (GFAAS) to determine the actual concentration before and after conducting the adsorption experiments. With a special hollow cathode lamp for arsenic detection and adjust the device settings to have a wavelength of 193.4 nm, slit 0.7 nm, and cell temperature of 900 C.

Small concentrations of elements, down to parts per billion of a gram, can be measured using GFAAS. this technique is based on the ability of an element to adsorb a light with specific wavelength that other elements cannot adsorb [70]. There are three phases to get a reading in GFAAS [71]: 1) Dry: in which the solvents, ultrapure water, is evaporated. 2) Ash, in which the volatile hydroxides, sulfates, carbonates are removed. 3) Atomize, atomization of remaining analyte.

4.3 Experimental Methods

4.3.1 Membrane Fouling

Membrane fouling is a physical process caused by the deposition of either a solution or a particle, onto the surface of membrane resulting in a lower performance of this membrane. In this work, the effects of membrane fouling were observed by noting the differences in flux at constant pressure through the membrane before, during, and after interaction with foulants. Hydraulic flux is described as:

$$J = \frac{dV}{dt \cdot A} = \frac{\Delta P}{\mu \cdot Rt} \quad \text{(Equation 4.7)}$$

where J is permeate flux, V is the volume being filtered, A is the effective area of filtration, and t is time. In this manner, permeate flux can be determined by finding the

differential volumetric flowrate through the membrane and dividing by the effective area of the membrane surface. All membrane fouling experiments were carried out at pH (5.5 - 6) and in the absence of ionic strength, in order to isolate the interaction between the fouling material and the membrane surface.

4.3.1.1 Ultrafiltration cell set-up

Amicon millipore stirred ultrafiltration cell, model 8400, was used to conduct the membrane fouling experiments. The ultrafiltration cell was attached to an air cylinder, and a pressure difference of 10 psi was maintained during the experiment. The maximum capacity of the ultrafiltration cell is 350 mL. A volume of 300 mL was put into the ultrafiltration cell.



Figure 4-2:Amicon millipore stirred ultrafiltration cell.

4.3.1.2 Membrane's coating process

Three different types of coating materials were applied onto the surface of the membranes, ferroxane, 5% GO/IO-A composite material, and 10% GO/IO-A composite material.

A solution of 1000 ppm from ferroxane was prepared by dissolving 100 mg in 100 mL ultrapure water (18 M Ω .cm) then the ultrafiltration cell was used to deposit ferroxane particles

from the solution onto the surface of the membrane then the membrane was sintered at 410 °C inside a furnace.

Different methods were examined to coat the membranes with the composite materials. Firstly, similar to the ferroxane coating, a 1000 ppm of each composite material, 5% GO/IO-A and 10% GO/IO-A, was prepared, as discussed in **section 4.1.4**, then the ultrafiltration cell was used to deposit the composite particles from the solution onto the surface of the membranes then they were sintered at 410 °C inside a furnace.

Secondly, a solution of 500 ppm of ferroxane was deposited onto the surface of the membrane, to create an adhesive surface, followed by the deposition of the 1000 ppm solution of the composite materials. Altogether were sintered at 410 °C inside the furnace.

Thirdly, the same was done as in the second method except that the ferroxane layer was sintered at 410 °C before the deposition of the composite materials.

Fourthly, the composite materials were sintered at 410 °C before the deposition. Then 100 mg of the sintered materials were re-suspended in 100 mL ultrapure water (18 MΩ.cm) to get 1000 ppm solutions. Again, the materials and the supports were sintered at 410 °C inside the furnace.

Finally, a solution of 500 ppm from ferroxane was deposited onto the surface of the membrane, to create an adhesive surface, followed by the deposition of the 1000 ppm solution of the sintered composite materials. Altogether were sintered at 410 °C inside the furnace.

4.3.1.3 Permeability

Filtration experiments were carried out using the same ultrafiltration cell. The cell was connected to an air cylinder with a regulator to maintain a constant pressure of 10 psi. The effective area of filtration varied between 15 cm² and 17 cm². The permeability of both the supports and the membranes was determined by filtering ultrapure water (18mΩ), measuring the

volume of the accumulated permeate at constant pressure as a function of time and calculating the linear fit of the experimental data. Using this data, the permeability was calculated using Darcy's law (Equation 3.13). Permeability is defined as the inverse of resistance, and was computed using the following equation,

$$\kappa = \frac{1}{R_t} \quad \text{(Equation 4.8)}$$

Where κ is permeability and R_t is the resistance.

4.3.1.4 Membrane fouling observation

First, clean water flux was observed by running 100 mL of ultrapure water (18m Ω) through the membrane and recording the time at 10 mL intervals. Second, a 1 g/L solution of bovine serum albumin (BSA; Fischer, Pittsburgh, PA) was prepared with ultrapure water (18m Ω); the flux was observed by running the BSA solution through the membrane and recording the time at 10 mL intervals. The membrane was then subjected to hydraulic cleansing using ultrapure water (18m Ω) for 30 seconds. Clean water flux was again recorded by running ultrapure water (18m Ω) through the membrane and recording the time at 10 mL intervals; the ratio of the second clean water flux to the initial clean water flux is called the "recovered flux". The entire process is described by **Error! Reference source not found.** below[24].

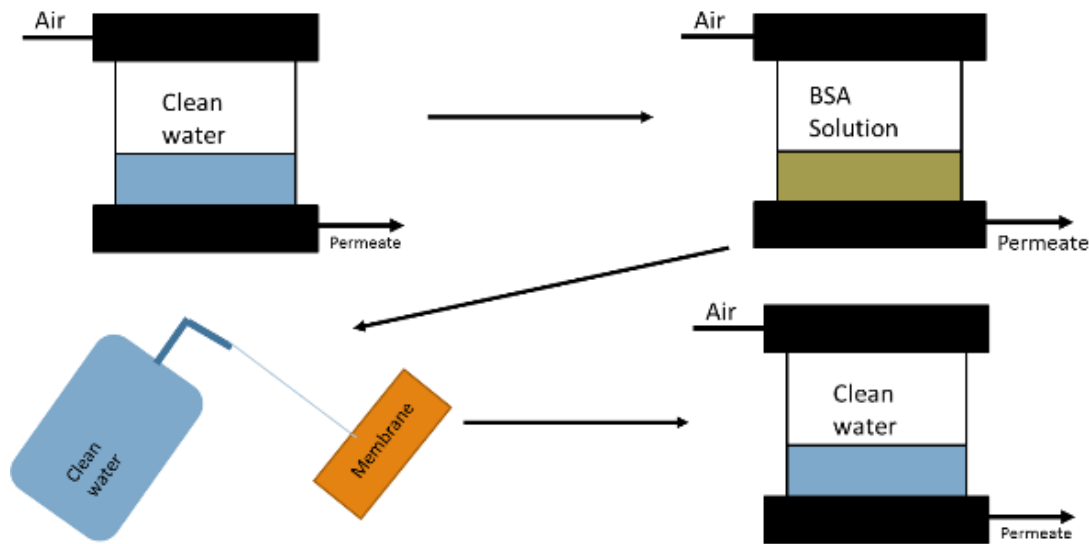


Figure 4-3: Schematic of the membrane fouling experiment [8].

4.3.2 Adsorption of arsenic

4.3.2.1 Adsorption isotherms for arsenic removal

Two major variables were applied and tested in this experiment, pH and ionic strength (IS). Four different conditions were simulated to examine the effects of each variable: (1) 1 mM IS, and pH 4.5. (2) 1 mM IS, and pH 7. (3) 100 mM IS, and pH 4.5. (4) 100 mM IS, and pH 7.

Ionic Strength 1 mM (pH 4.5, and pH 7):

A stock solution of As(v) (10 ppm, 1 mM) was prepared by dissolving 0.0416 g of Sodium Arsenate ($\text{Na}_2\text{HAsO}_4 \cdot 7\text{H}_2\text{O}$) and 0.085 g of Sodium Nitrate (NaNO_3) in 1 L of ultrapure water (18m Ω). Different concentrations of working solutions, 8, 6, 5, 3, 2, 1, and 0.5 ppm, were prepared from the stock solution using ultrapure water (18m Ω) with the same ionic strength (1mM) as the stock solution. Then, all solutions were adjusted to either pH 4.5 or pH 7 by adding NaOH or HCl. 50 ml of each solution was poured into a 125 mL flask. After that, a constant weight of the adsorbent material equals 20 mg was added to each flask. The flasks were sealed and shaken for 48 hours at 200 rev/min in a shaker. After shaking for 48 hours, samples were

filtered using 0.1 μm paper filters. All samples were preserved for analysis by adding 50 μL Nitric Acid then they were analyzed using GFAA device.

For Ionic Strength 100 mM (pH 4.5, and pH 7):

The same previous process was applied except this time the stock solution and the diluting ultrapure water have I.S. of 100 mM. To get this value, 8.5 g of NaNO_3 was dissolved in the 1L of the stock solution or the ultrapure water.

Note: all collected filtered samples were diluted to 100 ppb before analyzing them using the GFAA.

4.3.2.2 Adsorption kinetics

The preferable conditions for running the kinetics experiment was at pH 7 and I.S. 100 mM. So, a stock solution of As(v) (10 ppm, 100 mM) was prepared by dissolving 0.0416 g of Sodium Arsenate ($\text{Na}_2\text{HAsO}_4 \cdot 7\text{H}_2\text{O}$) and 8.5 g of Sodium Nitrate (NaNO_3) in 1 L of ultrapure water (18m Ω). Then, the pH was adjusted to reach 7 by the addition of HCl or NaOH. The 1L stock solution was divided into two halves and each half was poured in 1L well-sealed plastic bottle. Then, 0.5 g of adsorbents (5%, and 10% composites) were added to each bottle, separately. Before the addition of the adsorbents, a sample was taken from the stock solution. After the addition of the adsorbents, the bottles were sealed well and shaken for the time of the experiment. During the experiment, samples were collected at different times. First, the shaker was turned off and a 1 mL sample of the solution was taking after waiting for minutes until most the adsorbents settled. The sample was filtered using a syringe filter and saved for analysis.

Note: each collected filtered sample was diluted to 100 ppb, by taking 0.5 mL of the solution and dilute it with ultrapure water (18m Ω) in a 50 mL volumetric flask, before analyzing them using the GFAA.

4.4 Modeling

4.4.1 Adsorption kinetic models

Pseudo-first, pseudo-second order and Elovich were selected to fit the kinetic experiment results.

4.4.1.1 Pseudo-first-order kinetic model

The pseudo-first order or Lagergren kinetic model is based on the concentration of solution and adsorption capacity of solid [72], as described by equation 1:

$$\frac{dQ_t}{dt} = k_1(Q_e - Q_t) \quad (\text{Equation 4.9})$$

where Q_e is the adsorption capacity at state of equilibrium, Q_t is the adsorption at time t and k_1 is a rate constant.

The linear form of the solution is:

$$\ln(Q_e - Q_t) = \ln(Q_e) - k_1 t \quad (\text{Equation 4.10})$$

The rate constant k_1 can be determined from the slope by plotting $\ln(Q_e - Q_t)$ vs. t . The difference to a true first-order model is that Q_e normally should be calculated from the intersection with the vertical axis at $t = 0$ but in this case, it can be used an adjustable parameter [73, 74].

4.4.1.2 Pseudo-second-order kinetic model

The pseudo second order kinetic model is described in differential form by The differential equation for this model is shown in equation 3 with k_2 as the rate constant of pseudo-second-order adsorption [73, 75]

$$\frac{dQ_t}{dt} = k_2(Q_e - Q_t)^2 \quad (\text{Equation 4.11})$$

where k_2 is the second order rate constant. Linearized of the solution allows to obtain k_2 from the plot of t/Q_t as a function of t :

$$\frac{t}{Q_t} = \frac{1}{k_2 \times Q_e^2} + \frac{t}{Q_e} \quad (\text{Equation 4.12})$$

4.4.1.3 The Elovich kinetic model

The Elovich kinetic model was originally formulated to describe oxidation processes and later used it to develop the kinetic model for adsorption [76]:

$$\frac{dQ_t}{dt} = \alpha * e^{\beta * Q_t} \quad (\text{Equation 4.13})$$

where α is the initial adsorption rate and β as the desorption constant.

Solving this differential equation with the boundary conditions $Q_t = 0$ at $t = 0$ and $Q_t = Q_t$ at $t = t$ and with the assumption of $\alpha\beta \gg 1/t$, the equation can be linearized as [75, 77, 78]

$$Q_t = \frac{1}{\beta} \ln(\alpha * \beta) + \frac{1}{\beta} \ln(t) \quad (\text{Equation 4.14})$$

4.4.2 Adsorption Isotherms models

Langmuir, Freundlich and Temkin isotherm models were used in order to describe the behavior of the adsorption process that involves interaction of the adsorbing species, the adsorbate, with the surface hydroxyl groups on the iron oxide, the adsorbent.

4.4.2.1 Langmuir isotherm equation

Langmuir model assumes a homogeneous surface and only a monolayer uptake so adsorption can only occur at a finite number of locations. Furthermore there is no transmigration of the adsorbate, constant enthalpy and sorption activation energy [69].

The Langmuir equation is:

$$Q_e = \frac{Q_{max} * b * C_e}{(1 + b * C_e)} \quad (\text{Equation 4.15})$$

where Q_e is the adsorbed metal concentration, Q_{max} is the maximum specific uptake, C_e is the metal residual concentration in the solution and b is the ratio of adsorption and desorption rates.

This equation can be linearized which enables to calculate b and Q_{max} with experimental data from the isotherm experiment (Equation 4.16)

$$\frac{1}{Q_e} = \left(\frac{1}{b * Q_{max}} \right) \frac{1}{C_e} + \frac{1}{Q_{max}} \quad (\text{Equation 4.16})$$

4.4.2.2 Freundlich isotherm equation

The Freundlich isotherm, first introduced in 1906, can be applied to multilayer adsorption onto heterogeneous surfaces with non-uniform distribution of adsorption heat [79].

The isotherm is expressed by [69]

$$Q_e = K_f \times C_e^{\frac{1}{n}} \quad (\text{Equation 4.17})$$

with Q_e as the amount adsorbed, n as the adsorption intensity, K_f as the Freundlich constant and C_e is the residual concentration of the metal in the solution. Linearly, the equation is expressed as:

$$\log(Q_e) = \log(K_f) + \frac{1}{n} \log(C_e) \quad (\text{Equation 4.18})$$

4.4.2.3 Temkin isotherm equation

The Temkin isotherm [80] is derived by the assumption of a uniform distribution of binding energy and takes into account the adsorbent-adsorbate interactions, assuming that the heat of adsorption rather decreases linearly than logarithmic with coverage [69], as described by

$$Q_e = \frac{RT}{b_T} \ln(A_T) + \frac{RT}{b_T} \ln(C_e) \quad (\text{Equation 4.19})$$

where R is the universal gas constant, T the absolute temperature, b_T is a constant related to the heat of adsorption, and A_T is the equilibrium binding constant corresponding to the maximum binding energy. Whereas the Langmuir equation assumes a uniform energy of adsorption, the Temkin equation uses logarithmic relationship that takes into account the heterogeneous surface on which the adsorption energy decreases as the coverage increases [73].

5 Results and Discussion

5.1 Materials characterization

5.1.1 Materials Production

After following the production procedures discussed in Chapter 3, the produced materials were ferroxane, graphene oxide, and the iron oxide composite material, 5% GO/IO and 10% GO/IO, as shown in Figure 5-1.

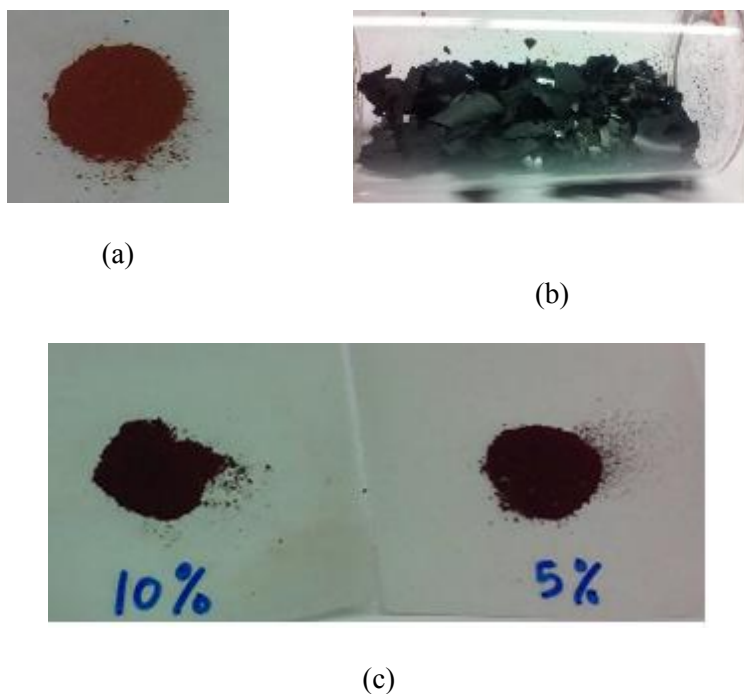


Figure 5-1: Produced materials: (a) Ferroxane, (b) Graphene Oxide (GO), (c) 5% GO/IO and 10% GO/IO composite materials.

One noticeable occurrence during the production process was the very fast aggregation rate when both ferroxane and GO were mixed together. The aggregation occurred immediately while pouring the GO solution into the ferroxane solution. Figure 5-2 shows different phases of aggregation for both composite materials.

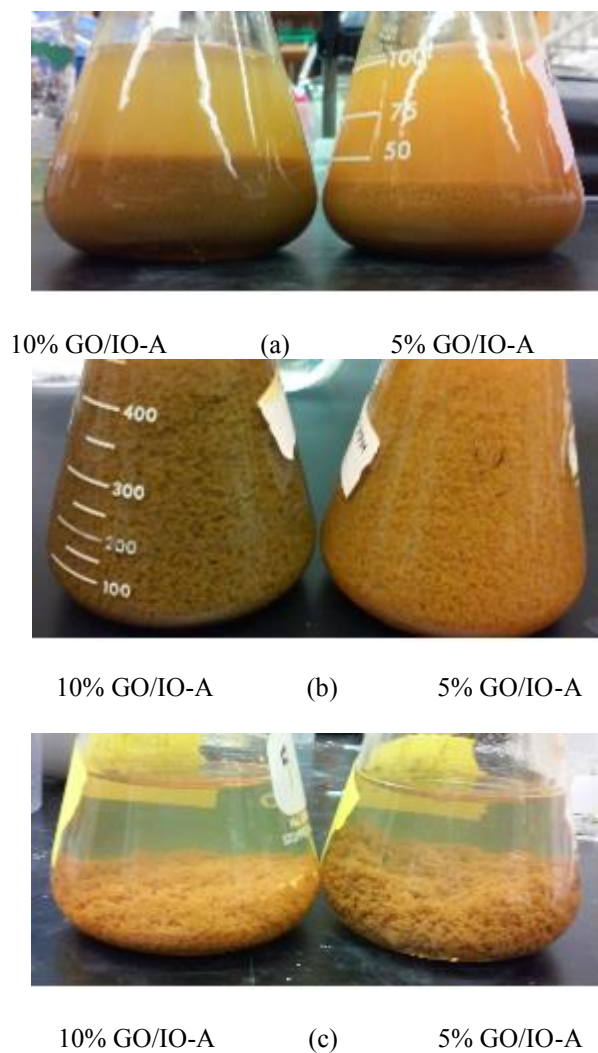


Figure 5-2: (a) Aggregates after few seconds of mixing both IO and GO, (b) Aggregates during stirring after approximately two minutes of mixing, (c) Settled aggregates after few minutes of stirring.

According to the observation, the aggregation rate for the 10% GO/IO-A composite material was faster than the one for the 5% GO/IO-A composite material, and the final aggregates were larger as well. Moreover, the color of the 10% GO/IO-A composite material was darker than the color of the 5% GO/IO-A composite material. This is due to the larger amount of GO nanoparticles that attracts more ferroxane nanoparticles in the case of 10% GO/IO-A composite material aggregation than the amount in the 5% GO/IO-A composite material, and it produced a darker color.

5.1.2 X-Ray Diffraction

X-ray diffraction was conducted on lepidocrocite, ferroxane, hematite and composite materials to confirm their identity. lepidocrocite, ferroxane, and hematite were measured previously by Max Storm and the results are shown in Appendix A [24]. Figure 5-3 shows the results of XRD for both composite materials.

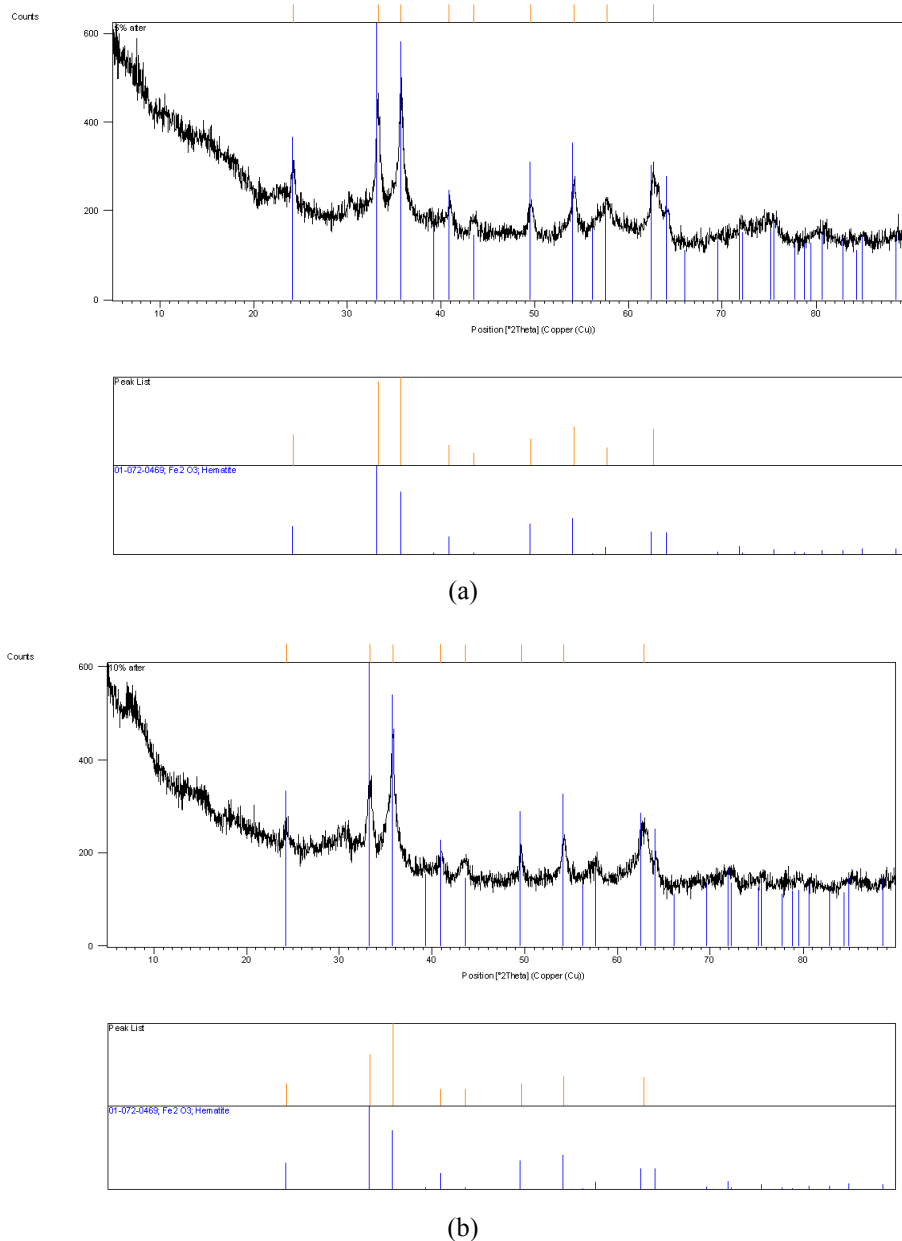


Figure 5-3: X-ray diffractogram for sintered (a) 5% GO/IO composite material, (b) 10% GO/IO composite material.

Both diffractograms have similar patterns, and meet, to a certain extent, the peaks of hematite diffractogram (peaks shown in blue). The highest peaks for both occurred at $\theta = 33^\circ$ and $\theta=35.5^\circ$. Thus, the addition of GO nanoparticles to ferroxane nanoparticles results in a slight change in the crystalline structure of the basic material, ferroxane. Even after the sintering process, both composite materials' crystalline structure was almost similar to the hematite.

5.1.3 Surface Charge

The measured zeta potential for GO in this work are in agreement with data in the literature (see for example Jian Zhao [61]). As shown in Figure 5-4, the zeta potential of GO was negative for all pH values, and it decreases as pH increases. The ionization of carboxyl and hydroxyl functional groups as pH increases is considered to be the major reason for this pH dependence of the surface charge of GO [81].

As for ferroxane, it was mentioned in Cornell's work [60] that lepidocrocite has a point of zero charge (pzc) ranging from pH 6.7 to pH 7.5; thus, the finding in this work regarding the zeta potential of ferroxane, pzc equals pH 7.8, is accurate and almost close to what was mentioned in previous works. At pHs less than pzc, the deprotonated functional groups dominate over the protonated ones, and at pH 7.8 both the positive and negative groups are equal.

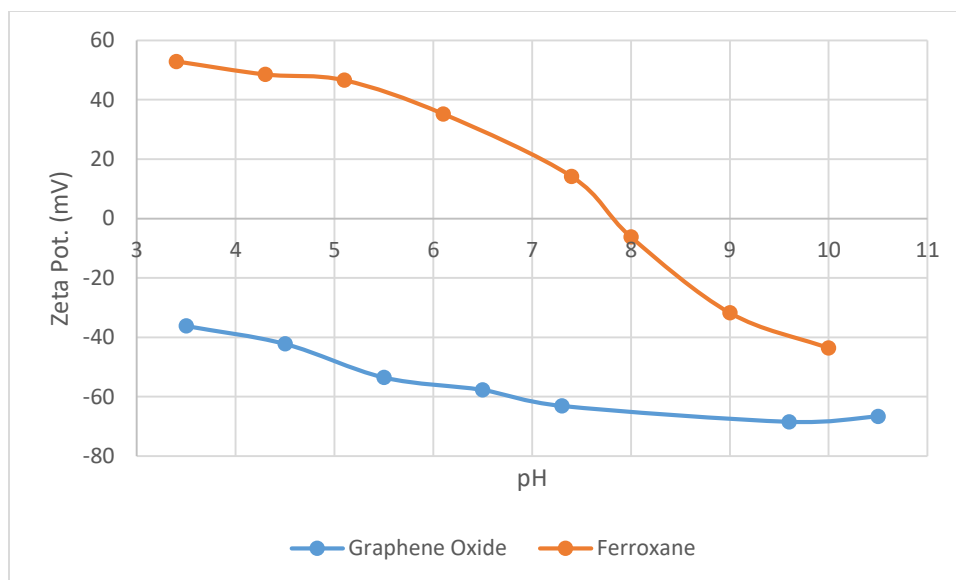


Figure 5-4: Zeta Potential for ferroxane and graphene oxide, suspended in ultra-pure water, as a function of pH.

The results of zeta potential for both ferroxane and GO can give a good indication for the best pH condition to combine both materials. There are two important factors that control the aggregation process and the condition of mixing should be favorable to enhance them to get fast aggregation. First, the electrostatic attraction is playing a major role in this process, and it will occur at pH values in which both materials have opposite surface charges. While the other factor is Brownian diffusion, which occurs for fine particles and it causes a collision between these small particles, so the stirring speed should be adjusted for Brownian diffusion to occur. In conclusion, the best range of pHs for combining ferroxane and GO is below the pzc of IO, below pH 7.8. To benefit from the maximum potential of the electrostatic attraction (maximum difference in charge between positive ferroxane and negative GO), I selected the pH condition below 6, and the speed of stirring about 100 rpm.

Zeta potential for the new composite materials gives information about their surface characteristics, and may be indicative of the potential of these materials in removing contaminants. Figure 5-5 displays zeta potential distribution for the sintered composite materials.

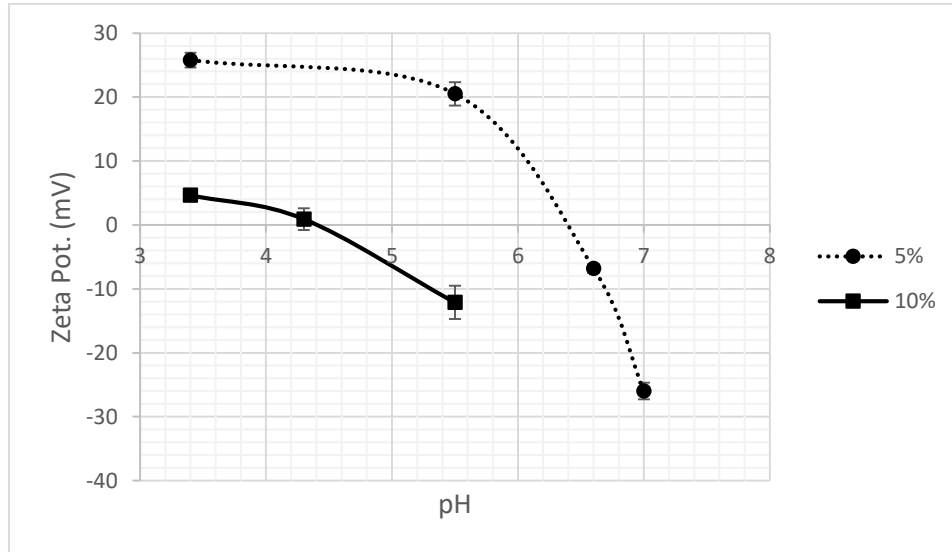


Figure 5-5: Zeta potential for the sintered 5% GO/IO and 10% GO/IO composite materials as a function of pH.

As expected, the amount of GO added to each composite material had a big impact on the evolution of surface charge for each composite material. Because more negative groups were added to the 10% GO/IO composite material by adding more GO, zeta potential starts with low value, almost 5 mV, at low pH and reaches pzc at pH 4.4 very fast. On the other hand, the smaller amount of GO added to the 5% GO/IO composite material didn't add a lot of negative groups, so the positive groups on IO still dominate, but the effect of this addition made the surface charge drop to half of what it was in the pure IO. The positive surface charge starts slightly decreasing while increasing pH from below pH 3 to pH 5.5 then it rapidly decreases to reach pzc at pH 6.4 and continues to the negative side. The reason behind this trend is as discussed before, more positive groups on IO occur at $pH < 5.5$ then the number of these groups starts to decrease as pH increases while the negative groups in both IO and GO start to increase

gradually making a double effect on the positive groups and pulling the surface charge sharply to the negative side.

Many attempts were tried to measure the surface charge of the aggregates before the sintering process, but none of them gave stable readings because of the fast aggregation and the machine kept giving error messages.

5.1.4 Surface Area

The specific surface area of the hematite nanoparticles formed after sintering ferroxane was determined using BET method and equals to $73.87 \pm 1.98 \text{ m}^2/\text{g}$. This value is in agreement with the surface area of hematite that was reported by Cornell, surface area of hematite formed by dehydroxylation of lepidocrocite at temperature $< 500 \text{ }^\circ\text{C}$ can reach up to $200 \text{ m}^2/\text{g}$ [60], and it is similar to the one obtained by Storms ($72.47 \pm 2.01 \text{ m}^2/\text{g}$) [24]. One important factor that affects the surface area of hematite is the way it was produced (including the raw materials, and the temperature), which affects the particle size and shape. Thus, any change in the amount of heat and time applied during the sintering process will change the structure and size of particles, and this explains the wide range of surface area values mentioned in Cornell's work ($< 5 \text{ m}^2/\text{g}$ up to $200 \text{ m}^2/\text{g}$) [60].

As for GO nanoparticles, the specific surface area was, also, determined using BET method and found to be $151.4 \pm 2.51 \text{ m}^2/\text{g}$. This value is significantly lower than the theoretical surface area of a single GO sheet ($2630 \text{ m}^2/\text{g}$) [82]. A major reason for this huge difference is the incomplete exfoliation during the sonication step. Other reported values showed that the GO has a surface area of 466 to $640 \text{ m}^2/\text{g}$ [9, 83]. These values are higher than the measured one in this work because the production methods are not the same, and the applied temperature in the outgassing process in BET calculation was at least 3 times higher than the applied temperature in this work ($100 \text{ }^\circ\text{C}$ to avoid the decomposition of GO).

Finally, the determined specific surface areas for 5% GO/IO, and 10 % GO/IO composite materials were 65.98 ± 0.38 and 68.03 ± 0.12 m^2/g , respectively. Unlike what was expected, the addition of GO nanoparticles to the IO caused a reduction in the specific surface area to less than the hematite. An explanation for this case is that the GO nanoparticles were reduced because of the high temperature (410 °C) applied during the sintering process resulting in losing many functional groups from the surface, and breaking down the structure of GO. Then, those broken particles blocked the pores of hematite.

There was no need to measure the surface area of the aggregates for both composites before the sintering process because the main objective is to study the final form of the composites and their properties.

5.1.5 SEM Imaging

SEM images were taken for the ferroxane nanoparticles to observe the surface morphology of the particles then compare it with the composite materials. Figure 5-6 shows irregular surface morphology with high surface roughness for ferroxane nanoparticle, which look like needles with a size that reaches almost 300 nm.

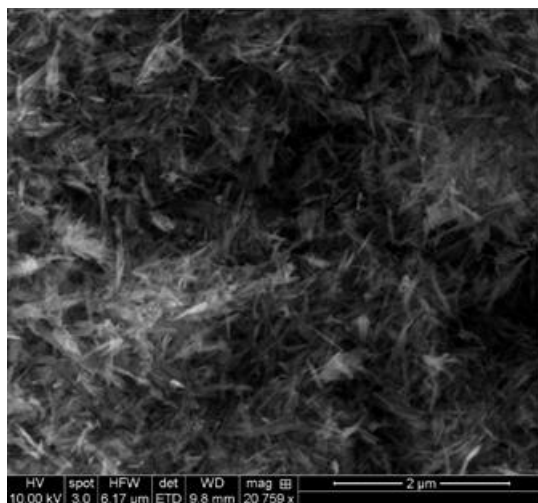


Figure 5-6: SEM image for ferroxane nanoparticles.

GO nanoparticles images were obtained using transmission electron microscope (TEM), see Figure 5-7. It is easy to see the GO nanoparticles look like sheets combined with each other. These sheets have sharp cut edges and in some areas several layers of sheets stacked and overlapped together. The roughly estimation of the size of each separate sheet is about 400 nm.

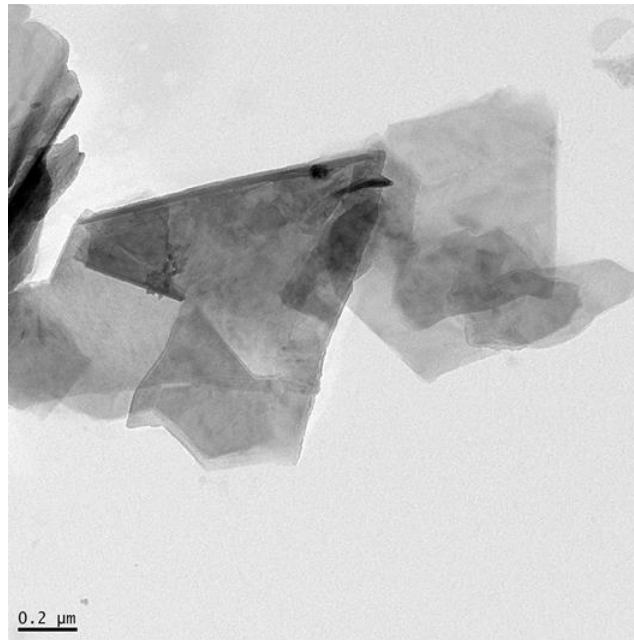


Figure 5-7: TEM image for GO nanoparticles (sheets).

As for both composites, images were taken from two different stages of the production , the first stage is while the composites are aggregates and before the sintering process while the second stage is after the sintering process. Images of the first stage was done after both composites were created from ferroxane and GO, but not sintered. Figure 5-8 gives a general view of the aggregates formed for both composites.

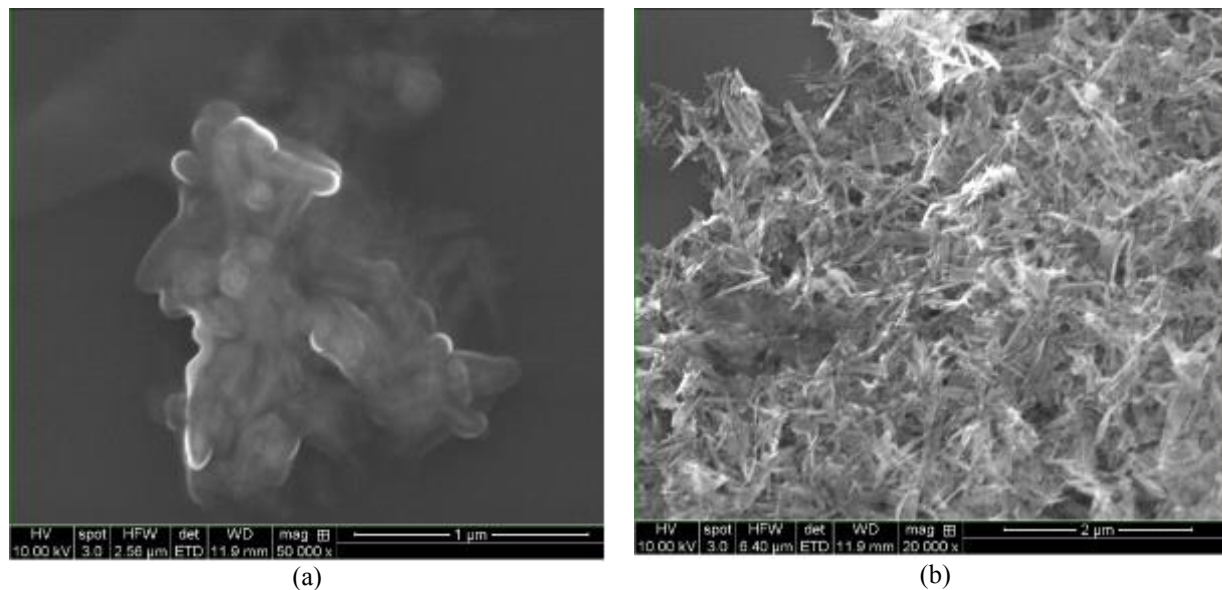


Figure 5-8: SEM images for suspended aggregates of (a) 5% GO/IO-A composite, (b) 10% GO/IO-A composite.

It was evident during the search for aggregates under the microscope that the aggregates in the 5% GO/IO composite tend to have a smaller size than the ones in the 10% GO/IO composite. The amount of GO added to the 10% GO/IO affects the rate and size of aggregates as it was discussed previously. It was proven that both ferroxane and GO were attached to each other as shown in Figure 5-8 (a). The GO sheets totally covered the ferroxane nanoparticles and helped in forming bigger aggregates. Additional measurements were carried out to assure that ferroxane and GO were mixed. Energy Dispersive Spectroscopy (EDS) was used to verify the type of elements that both composites consist of. Results are shown in Figure 5-9 and Figure 5-10.

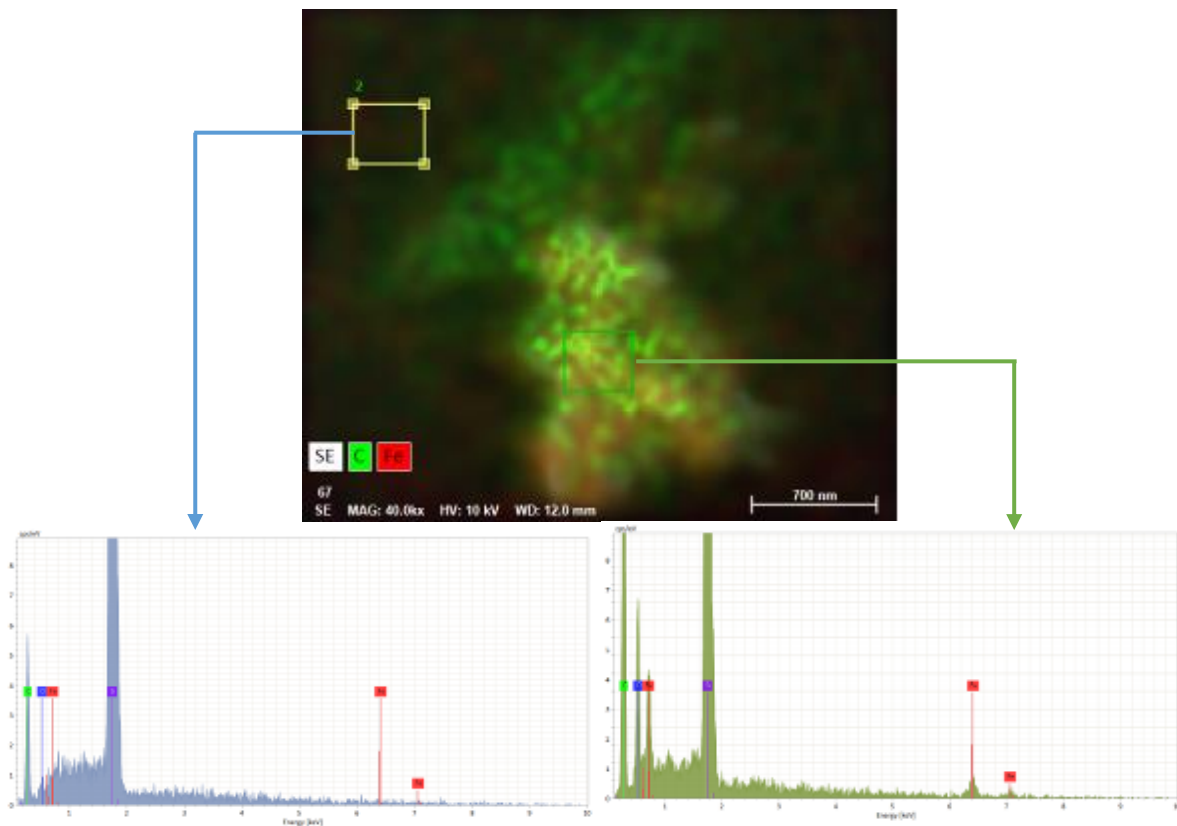


Figure 5-9: EDS analysis for the 5% GO/IO composite.

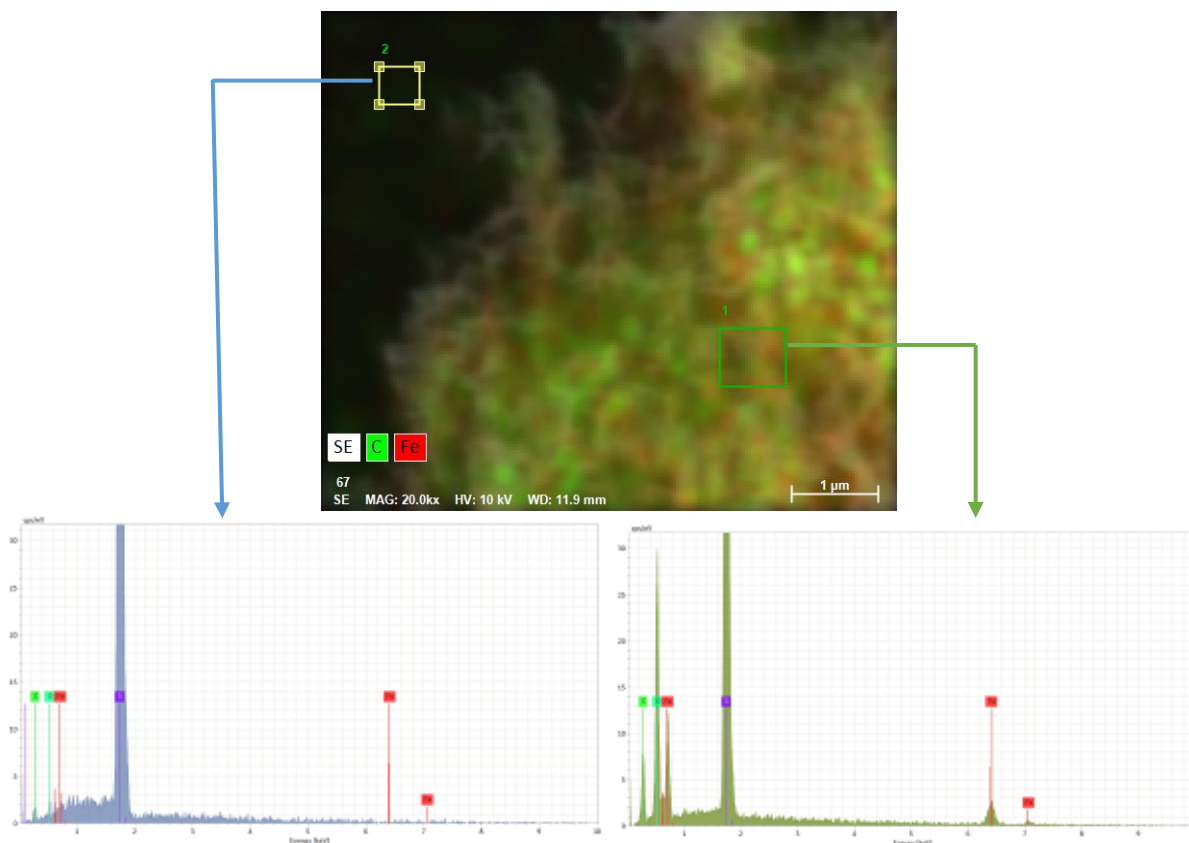


Figure 5-10: EDS analysis for the 10% GO/IO composite.

It is clear from the two analyses above that aggregates in both composites contain Fe element, indicator of ferroxane, and C element, indicator of GO, both of them mixed together. Some GO sheets were not attached to ferroxane as shown at the upper left corner in Figure 5-8 (a) and the analysis in Figure 5-9. This might have happened because the ferroxane nanoparticles were totally covered by GO sheets which prevent other sheets from being attracted to the ferroxane nanoparticles.

Images of the second stage was done after sintering the composite materials. Few SEM images were taken to look at the morphology of the new composites after being sintered at 410 °C, some of them are shown in Figure 5-11.

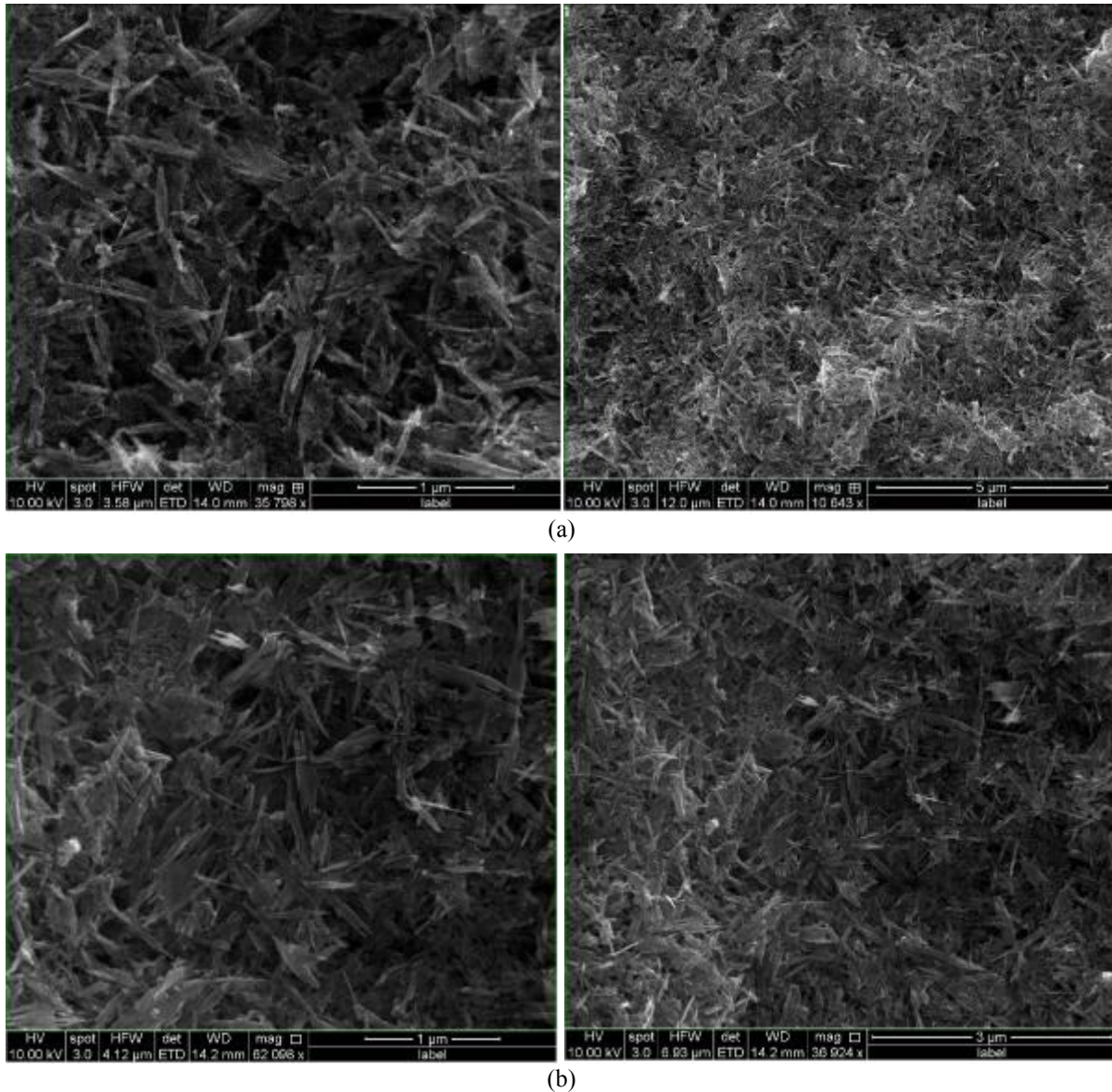


Figure 5-11: SEM images for sintered aggregates of (a) 5% GO/IO composite, (b) 10% GO/IO composite.

From these images, it was clear that there is no major difference between both composites and ferroxane. Therefore, composing both ferroxane and GO results in no change in the morphology of the basic material, ferroxane. It was shown, also, that there is no clear vision of the presence of GO. This might be due to the decomposition of GO, as a result of applying high temperature, and the destruction of GO bonds, reduction of GO start occurring at temperatures above 200 °C and the rich oxygen functional groups (carboxyl and hydroxyl) are

the first one to get destroyed [84]. This reason might be the main cause for the cracked and unattached surfaces of both composites after coating the membranes with them and sintering them, which will be discussed in the membrane fouling section.

During scanning the samples, some strange occurrences were noticed. In some parts of the composites' layers there were few holes on the surface of the layers, see Figure 5-12. These holes might have occurred because of the rapid released of the remaining water vapor trapped inside the layers as well as the release of other gases such as CO₂ from the decomposition of the functional groups.

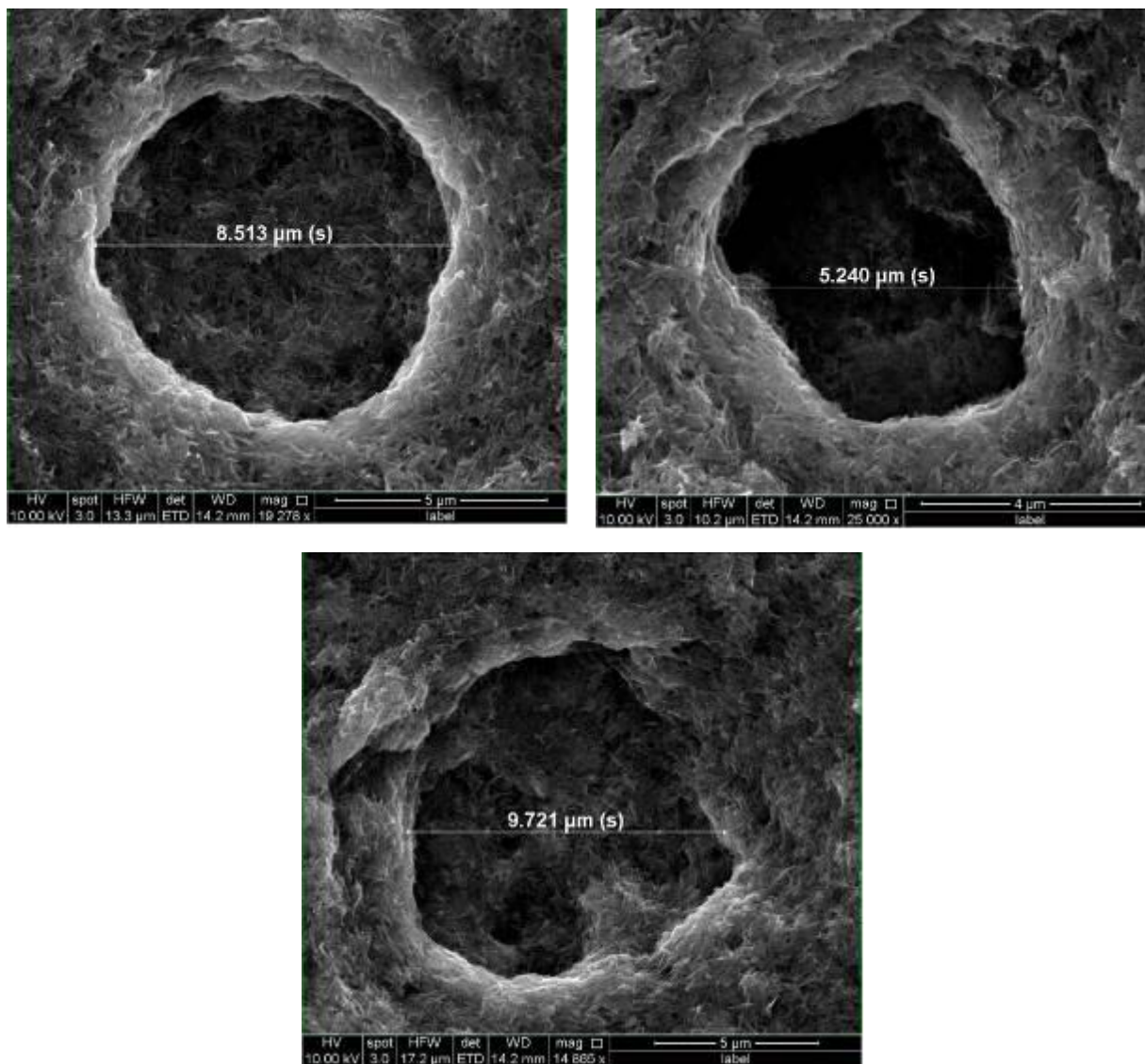


Figure 5-12: SEM images for strange holes in the surface of the composites.

5.1.6 Size

5.1.6.1 Dynamic light scattering method

As discussed before, DLS method was used to determine the size of ferroxane as well as GO before the composing process. Z-average, which is the intensity weighted mean hydrodynamic size of a group of particles, was found to be the representative measurement for DLS because of the stability of readings and the very low standard error. From Figure 5-13, Z-

average for GO exhibits, almost, a constant value of 280 nm as pH changes in the range of 3.5 to almost 10.

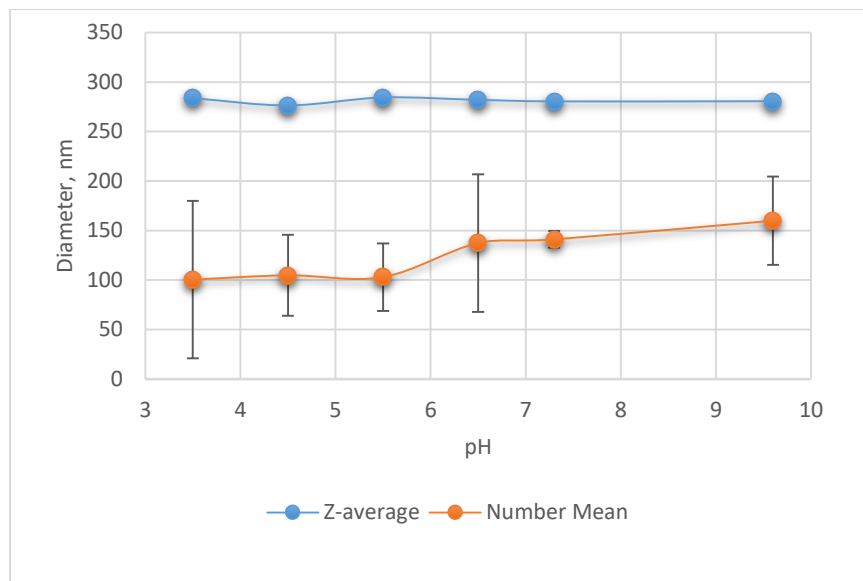


Figure 5-13: Z - average and number mean diameters distribution of GO with respect to pH.

A disturbance occurs in the readings outside this range of pHs, and an aggregation happens to GO sheets. The reason behind the formation of aggregates at low pH is related to the surface functional groups. Carboxyl groups are protonated at low pH, so GO sheets become less hydrophilic, and the electrostatic repulsion starts to decrease which allow the particles to overcome this force and form aggregates. At high pH, in contrast, the carboxyl groups are deprotonated making the GO sheets more hydrophilic, and more electrostatic repulsion occurs so particles tend to disperse in the solution by themselves [85].

As for ferroxane (Figure 5-14), Z-average shows a constant value of, almost, 270 nm for pH <5. Then, a sharp increase in the value occurred at pH \cong 6. For values above pH 6, aggregation and settling occurred to the ferroxane. The reason behind this aggregation is related to the decrease in the electrostatic repulsion forces between particles as they lose their surface

charge allowing Van der Waals attraction force to overcome the electrostatic repulsion force between particles allowing them to attach to each other and form the aggregates.

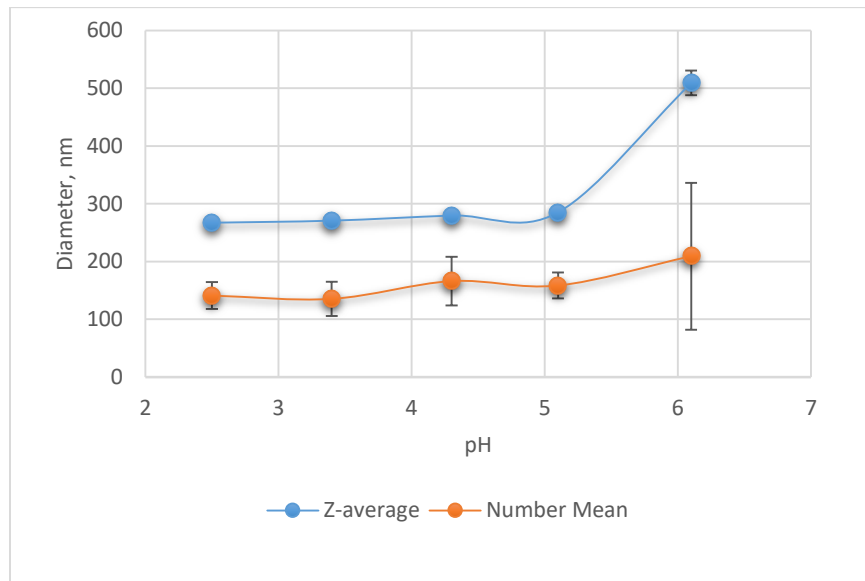


Figure 5-14: Z - average and number mean diameters distribution of IO with respect to pH.

5.1.6.2 SEM sizing

SEM method was used to determine the size of aggregates of the new formed composite materials before sintering. DLS is not an appropriate characterization method for those samples because the formed aggregates started to precipitate soon after the solution was injected inside the cell. In Figure 5-15, SEM images for both composite materials show that the aggregate size for both composites was relatively larger when drying the samples inside the oven than it was when drying at room temperature. The fast dehydration process for the samples in the oven results in disturbing the aggregates; therefore, collision occurred between the aggregates and thus larger aggregates were formed. In contrast, the slow and steady dehydration of the samples at room temperature leads to stable aggregates and prevents, to a certain extent, the collision of these aggregates; thus, aggregate sizes were relatively smaller.

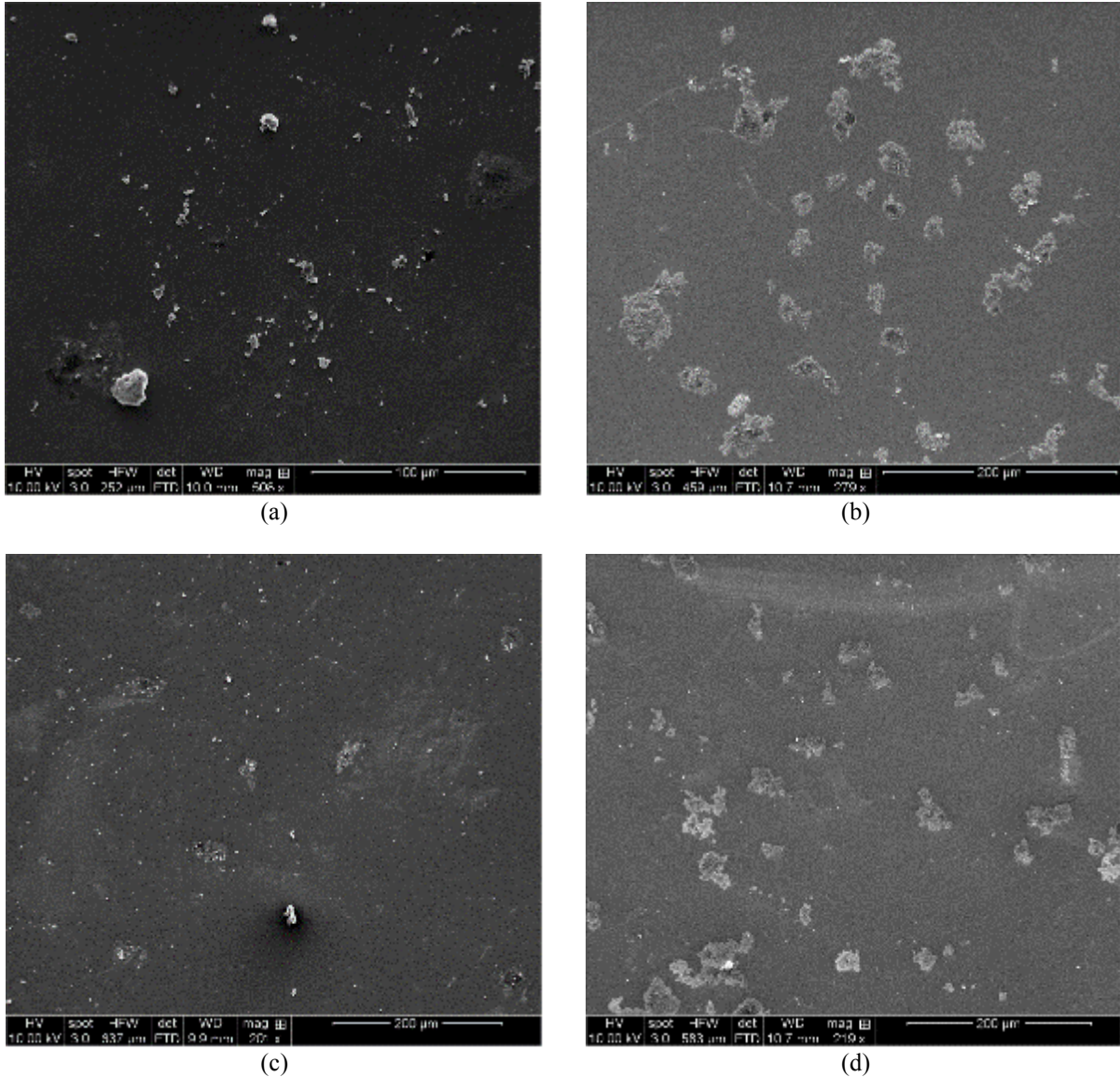


Figure 5-15: SEM images for composite materials (a) 5% GO/IO-A dried at room temperature, (b) 5% GO/IO-A dried inside an oven at 70°C, (c) 10% GO/IO-A dried at room temperature, (d) 5% GO/IO-A dried inside an oven at 70°C.

One of the methods to express size is measuring the mean diameter. The mean diameters of aggregates were measured from SEM images for both composites. The results are expressed by histograms. The data needed to draw these histograms are shown in Table 5-1 and Table 5-2. Figure 5-16 illustrate the diameters' frequency distribution of the aggregates' diameters while Figure 5-17 shows the diameters' cumulative distribution.

Table 5-1: 5% GO/IO-A aggregates' size data obtained from SEM.

Class boundaries (nm)	Class Mark $d_i(\mu\text{m})$	# Particles in class, n_i	Fraction of Particles in Class, f_i	# Particles of $d < d_i$	Fraction of Particles of $d < d_i = q_i$
0 - 10	5	11	0.172	11	0.172
10 - 20	15	18	0.281	29	0.453
20 - 30	25	19	0.297	48	0.750
30 - 40	35	8	0.125	56	0.875
40 - 50	45	5	0.078	61	0.953
50 - 60	55	1	0.016	62	0.969
60 - 70	65	2	0.031	64	1.000

Table 5-2: 10% GO/IO-A aggregates' size data obtained from SEM.

Class boundaries (nm)	Class Mark $d_i(\mu\text{m})$	# Particles in class, n_i	Fraction of Particles in Class, f_i	# Particles of $d < d_i$	Fraction of Particles of $d < d_i = q_i$
0 - 10	5	16	0.239	16	0.239
10 - 20	15	16	0.239	32	0.478
20 - 30	25	17	0.254	49	0.731
30 - 40	35	14	0.209	63	0.940
40 - 50	45	1	0.015	64	0.955
50 - 60	55	2	0.030	66	0.985
60 - 70	65	1	0.015	67	1.000

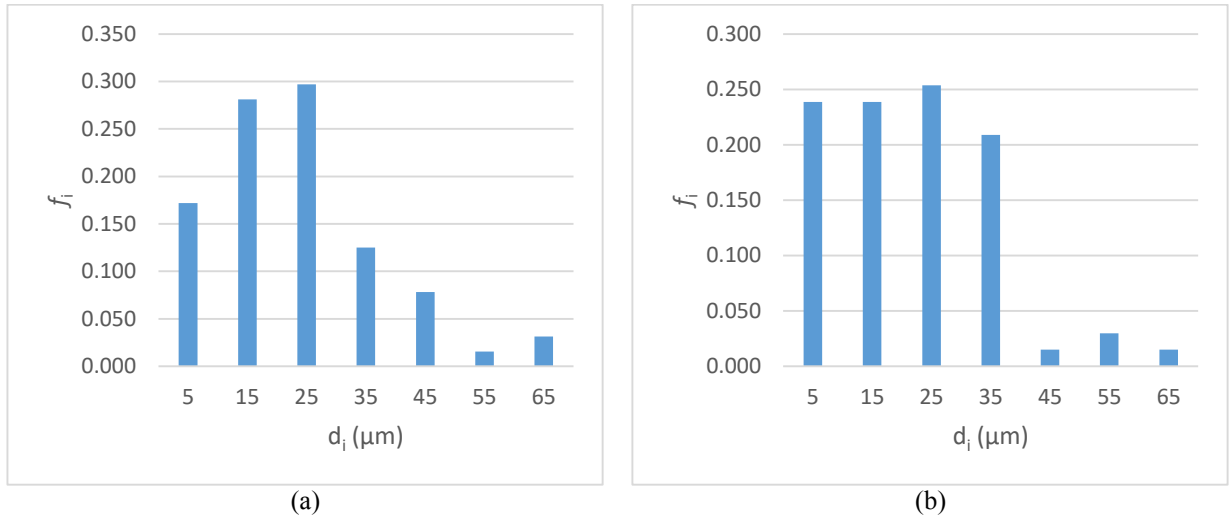


Figure 5-16: Histogram of the diameters' frequency distribution for composite material (a) 5% GO/IO-A, (b) 10% GO/IO-A

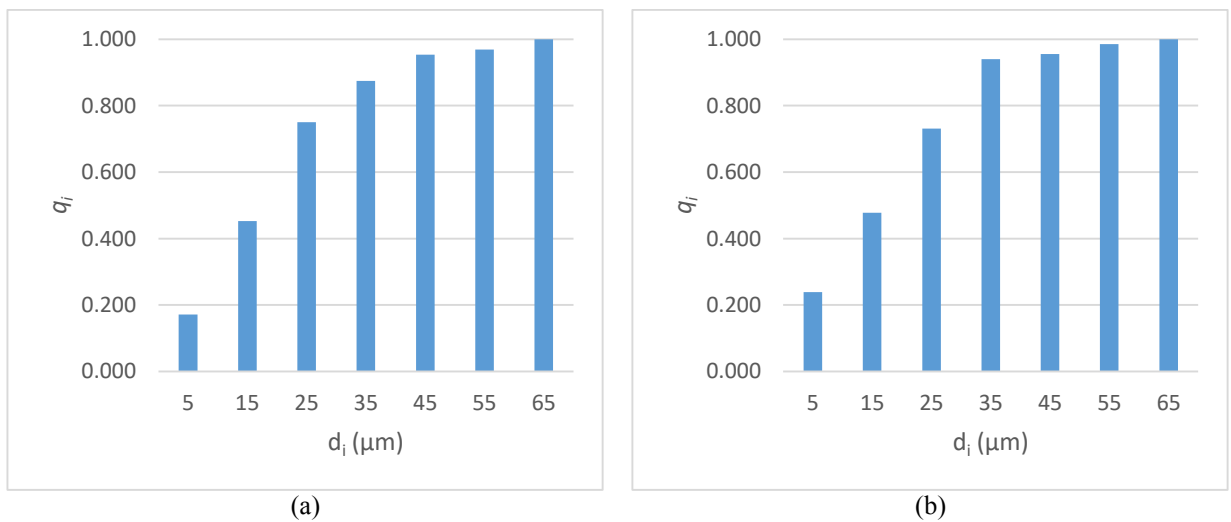


Figure 5-17: Histogram of the diameters' cumulative distribution for composite material (a) 5% GO/IO-A, (b) 10% GO/IO-A.

For the 5% GO/IO-A composite, more than half of the aggregates have diameters ranging between 15 – 25 μm while aggregates with diameters larger than 45 μm are rare. In contrast, aggregates of the 10% GO/IO-A composite have a very close distribution of diameters from 5 to 35 μm while aggregates with diameters larger than 35 μm are few. The reason for not observing

many aggregates with diameters greater than 35 μm for both composites can be related to the fast aggregation between larger aggregates to form small films as shown in Figure 4-18.

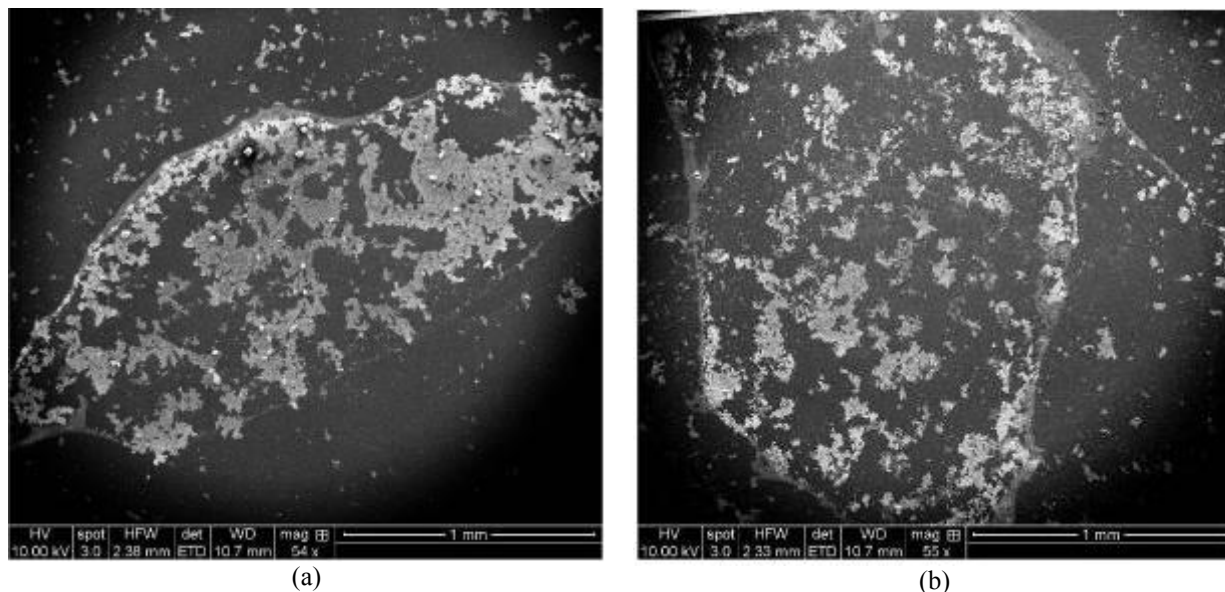


Figure 5-18: Films created by large aggregates of: (a) 5% GO/IO-A composite, (b) 10% GO/IO-A composite.

In sum, the main objective for measuring the aggregates' size is to find the smallest building unit that form bigger aggregates, and ultimately create the tiny films. The smallest aggregate size was found to be about 1 μm in diameter.

Studying particle size is important because it affects the adsorption process. The smaller the size of the particle, the more surface area with sorption sites is exposed to the solution which results in more adsorption capacity. The challenge is how to remove these small particles from the system if they are so fine and suspended in water. On the other hand, larger particles have less sorption sites exposed to the solution, which means less adsorption capacity, but these large particles can easily settle and be removed from the system. The composites obtained in this work tend to form large aggregates in a rapid way and settled very easily so that they can be removed from the systems without exerting much effort.

5.2 Membrane Fouling Characterization

The second objective of this work was to measure the fouling properties of the new composites to examine how they interact with contaminations and amount of recovery that can be obtained and how easy will be the washing process to make sure that these materials are suitable to increase the performance of the ceramic membranes.

The first step to characterize the membrane fouling was to measure the permeability of the alumina supports alone. Then, the surface of some supports was coated by ferroxane, and other supports by the composite materials separately. Next, all coated supports were sintered according to the program mentioned in section 4.1.4. Finally, the coated supports were tested for fouling.

Ferroxane coated supports were created in good conditions of stability and attachment to the supports' surfaces, Figure 5-19. Unfortunately, this work was suspended because the coating layers from both composites cracked and did not attach to the surfaces of the supports, Figure 5-20.



Figure 5-19: pure ferroxane coated supports after sintering.



(a)



(b)



(c)

Figure 5-20: (a) 10% GO/IO-A composite layer peeled after drying at room temperature for 24 hours. (b) 5% GO/IO composite layer cracked after sintering. (c) 10% GO/IO composite layer produced by the fifth method.

All the five methods that were explained in membrane coating section 4.3.1.2 gave unstable surfaces that cracked immediately after the deposition process or after the sintering process. But the fifth method, sintered composites were deposited on non-sintered ferroxane layers, gave the best results with a semi solid surface, but it cracked and start peeling when it was washed by DI water, Figure 5-20 (c).

The fifth method showed quite improvement because the composites were already sintered and they took their final shape. Thus, combining the composites' particles was achieved to a certain extent, but it was not fully stable because the bonds between the particles was still weak. My suggestion for a further work is to set up a new system in which the loose composites' particles are deposited directly onto the surface of ceramic membrane and running the fouling experiment. As for the washing process, it will be easy to collect the composites by applying magnetic field rather than backwashing for the ceramic membrane. After that, the composites can be redistributed onto the surface of the membrane after turning off the magnetic field.

5.3 Adsorption of Arsenic

5.3.1 Adsorption isotherms of arsenic

The experimental results of the adsorption isotherms for arsenic removal obtained under different conditions are shown in Figure 4-21. All experiments were conducted at room temperature (22 °C).

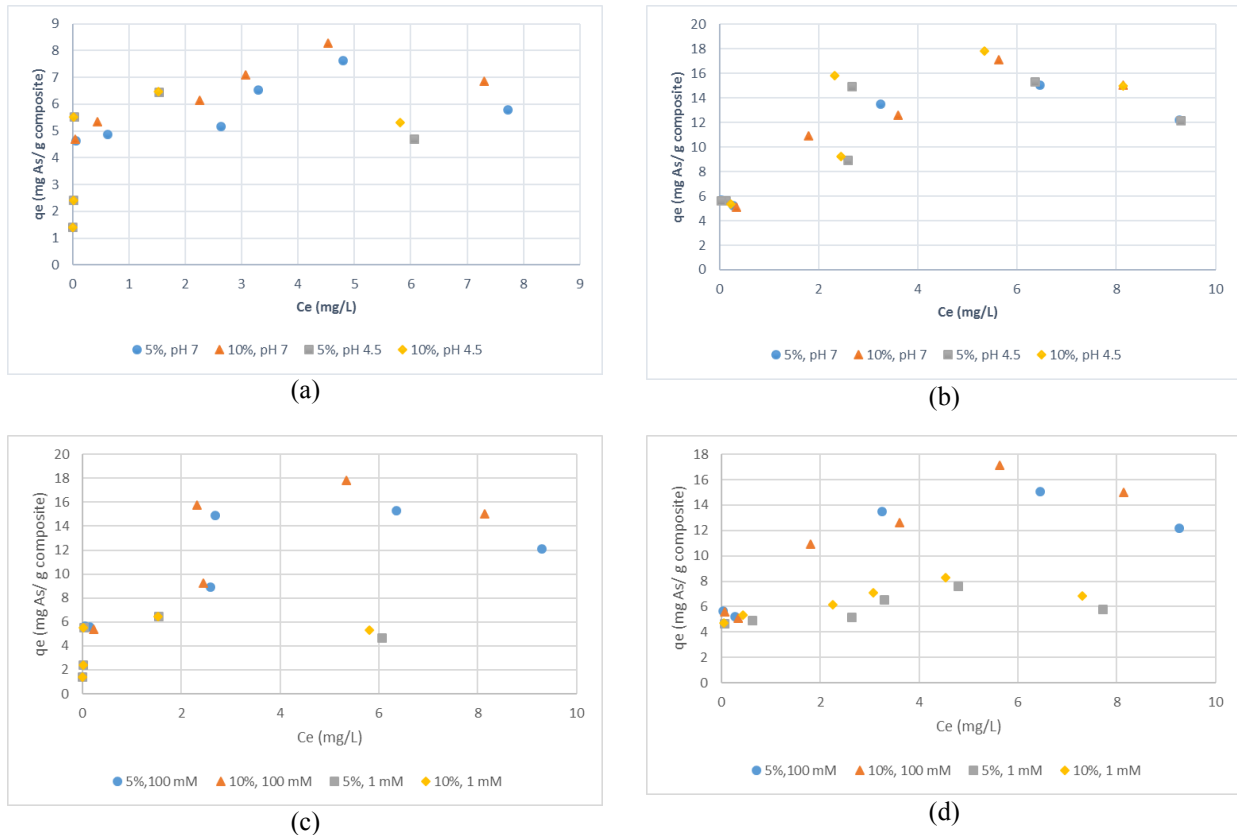


Figure 5-5-21: Adsorption isotherms for arsenic, effect of pH and ionic strength. at (a) IS 1 mM, (b) IS 100 mM, (c) pH 4.5, and (d) pH 7; [As(v)] is between 0.5 and 10 ppm, and [adsorbent] is 400 ppm.

In all the experiments, both composites display, to a certain point, similar patterns (the increase or decrease of q_e). Overall, the 10% GO/IO composite showed a slightly higher capacity in removing arsenic than the 5% GO/IO composite. All figures demonstrated a strange situation which is the decrease of the adsorption capacity at higher residual concentrations of arsenic.

5.3.1.1 Effect of pH

Figure 5-21 (a) & (b) present the influence of pH on the adsorption of arsenic onto both composites while the IS is constant. Both composite materials showed a higher affinity to adsorb arsenic at pH 7 when the IS is 1 mM, Figure 5-21 (a). However, at IS 100 mM, the composites exhibited close values for both pH 4.5 and pH 7. This means that the change in pH has a slight effect on the adsorption process at higher IS.

Generally, the experiments revealed unexpected results. Most researchers verified in their works that the adsorption capacity decreases as pH increases, which was discussed in the literature review. The surface of composites should be rich with hydroxyl groups, that arsenic tends to replace them during the adsorption process, at low pH; thus, the adsorption should be higher at low pH (in which more hydroxyl groups occurs) than at high pH (in which less hydroxyl groups occurs). However, the two composites exhibit a different pattern regarding the adsorption and pH changes. They showed slightly higher adsorption capacity at pH 7 than at pH 4.5.

Arsenic at $\text{pH} < 8.2$ is negatively charged according to the discussion in the literature. Also, according to the measured pzc of both composite, the 5% GO/IO composite was positive at pH 4.5 while the 10% GO/IO composite was slightly negative, but at pH 7, both of them were negatively charged. This helped the 5% GO/IO composite to adsorb more arsenic (depending on the electrostatic attraction) than the 10% GO/IO composite at pH 4.5, but still the adsorption of the composites increased or stayed the same when pH increased while it should be less due to the electrostatic repulsion between the negative ions of arsenic and the negative composites' nanoparticles.

5.3.1.2 Effect of Ionic Strength (IS)

Figure 5-21 (c) & (d) present the influence of IS on the adsorption of arsenic onto both composites while the pH is constant. Obviously, in case of high IS (100 mM), the adsorption increased twice as it was in case of low IS (1 mM). Thus, IS is a major factor in the adsorption process in this work. This, also, contradict what was mentioned in the literature. Adsorption is not affected by the electrostatic interactions (regulated by the IS of the solvent) [21].

5.3.1.3 Adsorption isotherm Modeling

Table 5-3 summarizes the best fitting model among the three models discussed in section 4.4. To see the linear regression for each model applied for each condition, see Appendix B.

Table 5-3: Best fit models with their parameters for different conditions.

Condition	Composite	Best fit model	R ²	n	K _f	Q _{max}	b
pH 4.5; IS 1 mM	5% GO/IO	Langmuir	0.932	-	-	6.05	45.917
	10% GO/IO	Langmuir	0.894	-	-	8.078	28.136
pH 7; IS 1 mM	5% GO/IO	Freundlich	0.52	11.047	6.14	-	-
	10% GO/IO	Freundlich	0.798	12.771	5.493	-	-
pH 4.5; IS 100 mM	5% GO/IO	Freundlich	0.807	5.277	9.29	-	-
	10% GO/IO	Langmuir	0.883	-	-	15.314	2.316
pH 7; IS 100 mM	5% GO/IO	Freundlich	0.812	3.983	9.277	-	-
	10% GO/IO	Freundlich	0.86	5.225	9.158	-	-

According to Table 5-3, most of the models do not have high good fit. There are few reasons why better fitting parameters were not accomplished. One main reason can affect the measurements is the instrumental error. Another one is the human error especially during the preparation of different concentrations and weighing the adsorbents.

The table shows that the most common adsorption model is Freundlich model. This means that the adsorption of arsenic onto the surfaces of the composite materials is considered to be a multilayer adsorption with non-uniform distribution of adsorption heat. Figure 5-22.

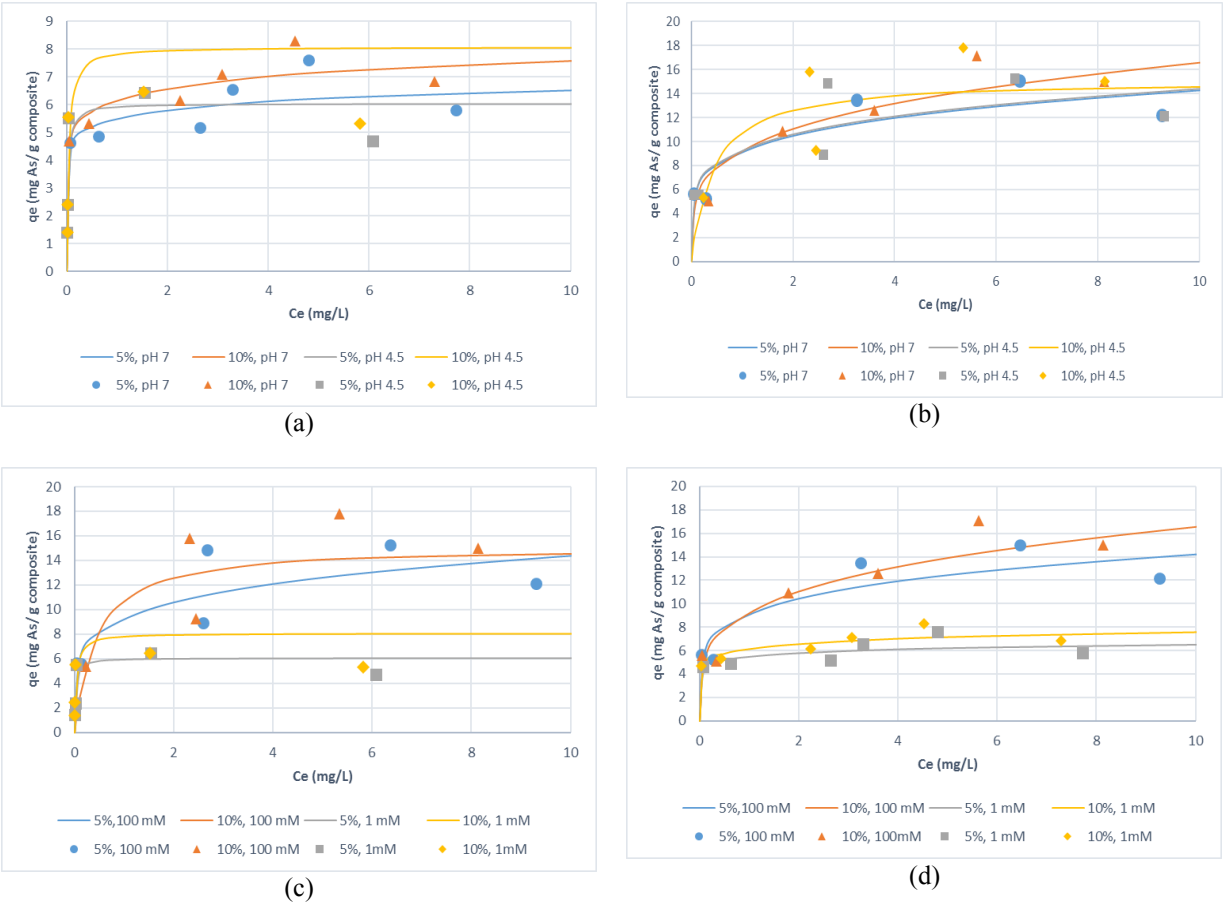


Figure 5-22: Non-linear regression models for arsenic removal at arsenic at (a) IS 1 mM, (b) IS 100 mM, (c) pH 4.5, and (d) pH 7; [As(v)] is between 0.5 and 10 ppm, and [adsorbent] is 400 ppm.

Even though the linear fitting of Langmuir model with the experimental data was the best fit at pH 4.5 and IS 1mM for the 10% GO/IO composite, the non-linear model gave higher values than the actual ones.

5.3.2 Adsorption Kinetics

5.3.2.1 Experiments' results

The results of the adsorption kinetic experiments for arsenic are illustrated in Figure 5-23. Both composites showed a rapid initial adsorption for arsenic at the start of the experiment. Yet, the 5% GO/IO composite's adsorption was faster than the 10% GO/IO during the first 2 hours. More than 50% of arsenic concentration was adsorbed during the first half hour by the 5% GO/IO composite while it took the 10% GO/IO composite one hour to adsorb 50% of the arsenic from the solution. After two hours, the 10% GO/IO composite started to adsorb more arsenic than the 5% GO/IO composite with 60% of arsenic was adsorbed. While the experiment continued, the adsorption kinetic started to have a slight decrease in arsenic removal percentage. It took almost 14 hours for both composites to adsorb additional 10% GO/IO of the original arsenic concentration.

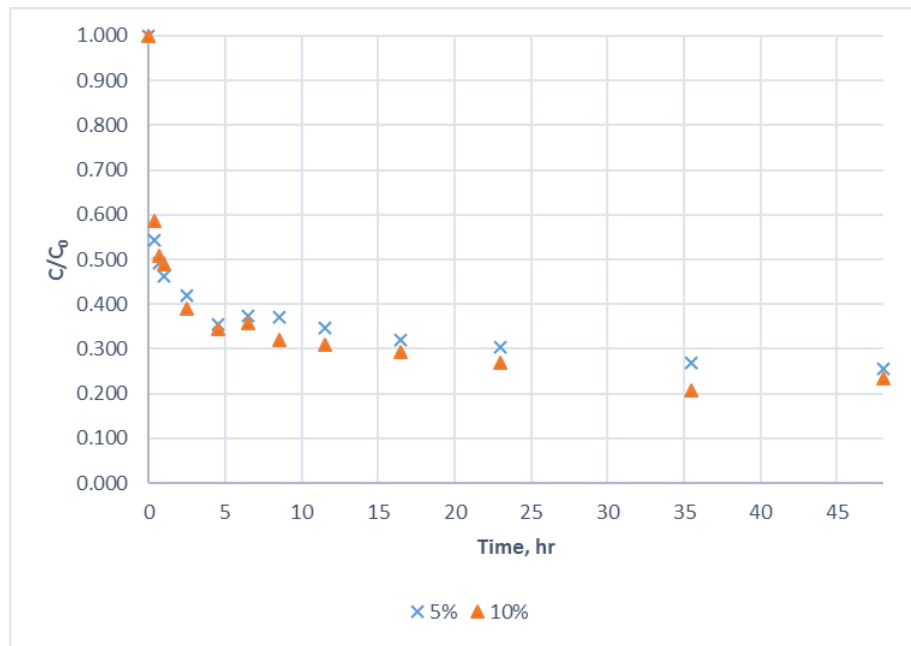


Figure 5-23: Adsorption kinetic of arsenic removal at pH 7 and IS 100 mM for both composites.

In summary, it was proven by the kinetic experiments that both composites need a short contact time to remove high percentage of the capacity.

5.3.2.2 Adsorption kinetics Modeling

The pseudo-first order and the pseudo-second order kinetic models were applied to fit the data by non-linear regression. For both composites, pseudo-second order kinetic model, Figure 5-24, was the best fit for the data in its linear form with R^2 values of 0.9985, and 0.9982 for the 5% GO/IO and 10% GO/IO composites, respectively. See Appendix C for the linear fitting of data by both models.

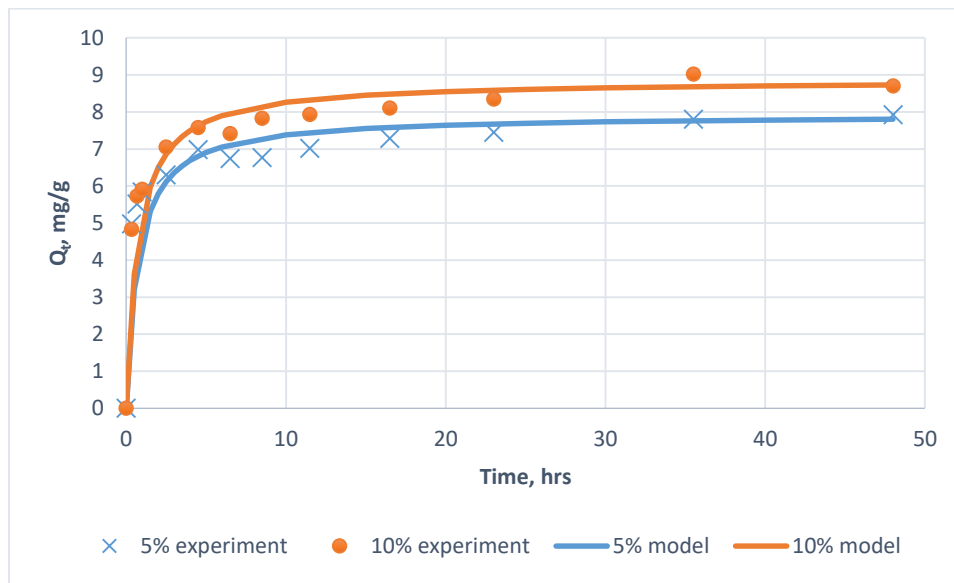
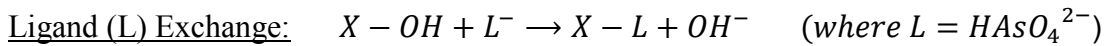
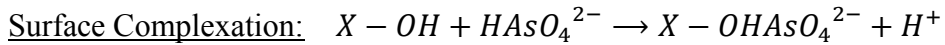


Figure 5-5-24: Non-linear pseudo second-order kinetics method and experimental kinetics for arsenic adsorption by both composites at pH 7 and IS 100 mM.

5.3.3 Adsorption Mechanism

As discussed in Chapter 3, functional groups, especially the hydroxides, attached to surfaces of IO and GO play a major role in the adsorption of arsenic. Arsenate, the source of As(V), embody both metal (As) and ligand (O) properties; therefore, the mechanisms of As(V) adsorption onto iron oxide surfaces can occur through surface complexation or ligand exchange, but the adsorption process of As still not fully understood [86].



In the first case, surface complexation, two of the four As–O bonding structures are complexed to Fe atoms (i.e., As–O–Fe) and the remaining two are present either both as unprotonated As–O or one as unprotonated As–O and the other one as protonated As–O–H [87]. A decrease in the solution pH would be a good indicator in this case as more H⁺ ions are released into the solution. On the other hand, the indicator for a ligand exchange of As(V) with OH⁻ is the increase of the solution pH [88].

It is expected that the previous two mechanisms can be applied only for hematite (IO) because GO lost most of the hydroxyls functional groups after the high temperature exerted during the sintering process. Also, it is expected that inner sphere complexations process is predominating the ligand exchange process as a representative mechanism for As adsorption onto the IO/GO composites because the pH during the experiments dropped slightly. However, Hoan, Thu, and Duc verified in their work that the addition of GO to the iron oxide (Fe₃O₄) improves the adsorption of many heavy metals such as As(V), Ni(II), and Pb(II) [89]. Yet, they didn't propose a clear explanation on the adsorption's mechanism. In another research, it was found that the addition of GO to other metal oxides (manganese oxide) helped in increasing the adsorption capacity for Pb(II)[90]. According to this research, the abundant

negatively charged groups attached to the surface of GO enhanced the separation of the ions through Donnan membrane effect. The Donnan effect relates to the behavior of charged particles near a semi-permeable membrane that can be used to separate unwanted ions [91]. However, since this work investigated the adsorption of negative ions, As(V), the aforementioned mechanism does not seem to apply Donnan membrane effect as a proposed mechanism for our IO/GO composites. More generally, the common finding between the previous two researches and the current work is the fast kinetics of the adsorption and reaching the equilibrium in a short time by the addition of GO.

According to this work's results, As(V) adsorption onto the surface of IO is strongly influenced by changes in ionic strength while it is less influenced by changes of pH in the range between pH 4 and pH 7. This is in a disagreement with the results obtained by many researchers such as Yannick and Sabbatini [16, 92].

6 Conclusions

Raw materials were produced with some differences between the obtained hematite in this work and in other works because a different method was used to produce it. Also, the composite material was successfully synthesized in two different ratios. Both raw materials and composites were examined and most of their properties were measured. In short,

- The temperature applied to convert ferroxane to hematite was 410 °C, and it was the same to sinter the composites.
- The highest two peaks in the XRD analysis for both hematite and composites occurs at $\theta = 33^\circ$ and $\theta = 36^\circ$. Thus, the crystalline structure of hematite does not change by the addition of GO.
- Average specific surface areas for hematite, GO, 5% GO/IO, and 10% GO/IO were 73.87 ± 1.98 , 151.4 ± 2.51 , 65.98 ± 0.38 , and 68.03 ± 0.12 m²/g, respectively.
- Ferroxane has pzc at pH 7.8 while GO has a negative charge at all pH values. Thus, the preferred aggregation between both of them occurs at pH below pH 6.
- SEM images did not reveal any change in the shape of hematite after the addition of GO.

Thus, the first objective of this work, preparing and characterizing the raw materials and the new composites, was positively accomplished.

On the other hand, the second objective could not be accomplished due to the unstable and broken composites' layers that occurred before and after the sintering process. Thus, no data was obtained regarding the fouling properties of the new composites.

Finally, the highest adsorption capacity occurred for the 10% GO/IO composite at pH 7 and ionic strength 100 mM (almost 18 mg A(v)/g adsorbent) which is strange because the

suitable pH condition for effective arsenic removal by adoption should be at low pH according to literature. The kinetics experiments demonstrated a rapid sorption process that almost 60% of As(v) was adsorbed by both composites after two hours while the saturation occurred after 17 hours with 7.9 mg/g, 8.8 mg/g and for the 5% GO/IO and 10% GO/IO composites, respectively. Freundlich model was found to be the best fit for many adsorption isotherms while the remaining ones were fitted by Langmuir model. The pseudo second-order kinetics model was the best non-linear model to fit the adsorption kinetics results data. In general, increasing the percentage of GO in the composites results in a small increase in the adsorption capacity. By this, the third objective was successfully accomplished.

7 Further works

Additional work needs to be done in investigating the adsorption capacity at higher saturation concentrations of arsenic to make sure that the capacity is not actually decreased as the adsorption isotherms experiments' results displayed. Moreover, there is a big need to investigate the mechanism of arsenic adsorption at high pH to further confirm the obtained results in this work.

One thing to add, the composites displayed some sort of magnetic property that was discovered before the completion of the work, and there was no time to characterize this property. Thus, a further investigation should focus on this property and how to benefit from it in water treatment.

Other than arsenic, adsorption of heavy metals such as lead, cobalt, and copper by the new composites should be investigated and compare the results with other works to support the validation of this new composite as adsorbent material in the field of water treatment.

8 References

1. Welch, A.H., et al., *Arsenic in ground water of the United States: occurrence and geochemistry*. Ground water, 2000. **38**(4): p. 589-604.
2. Nordstrom, D.K., *Worldwide occurrences of arsenic in ground water*. Science, 2002. **296**(5576): p. 2143-2145.
3. Smith, A.H., E.O. Lingas, and M. Rahman, *Contamination of drinking-water by arsenic in Bangladesh: a public health emergency*. Bulletin of the World Health Organization, 2000. **78**(9): p. 1093-1103.
4. Petrusovski, B., et al., *Arsenic in drinking water*. Delft: IRC International Water and Sanitation Centre, 2007. **17**(1): p. 36-44.
5. Pirnie, M., *Technologies and costs for removal of arsenic from drinking water*, in *Technologies and costs for removal of arsenic from drinking water*. 1999, EPA.
6. Clifford, D.A., *Ion exchange and inorganic adsorption*. Water quality and treatment, 1999. **4**: p. 561-564.
7. Mohan, D. and C.U. Pittman, *Arsenic removal from water/wastewater using adsorbents—a critical review*. Journal of hazardous materials, 2007. **142**(1): p. 1-53.
8. Hegab, H.M. and L. Zou, *Graphene oxide-assisted membranes: Fabrication and potential applications in desalination and water purification*. Journal of Membrane Science, 2015. **484**: p. 95-106.
9. Zhu, Y., et al., *Graphene and graphene oxide: synthesis, properties, and applications*. Advanced materials, 2010. **22**(35): p. 3906-3924.
10. Chandra, V., et al., *Water-dispersible magnetite-reduced graphene oxide composites for arsenic removal*. ACS nano, 2010. **4**(7): p. 3979-3986.
11. Sreepasad, T., et al., *Reduced graphene oxide–metal/metal oxide composites: facile synthesis and application in water purification*. Journal of hazardous materials, 2011. **186**(1): p. 921-931.
12. Zhang, K., et al., *Graphene oxide/ferric hydroxide composites for efficient arsenate removal from drinking water*. Journal of hazardous materials, 2010. **182**(1): p. 162-168.
13. Liang, Y., et al., *TiO₂ nanocrystals grown on graphene as advanced photocatalytic hybrid materials*. Nano Research, 2010. **3**(10): p. 701-705.
14. Xie, J., et al., *Fabrication of TiO₂-graphene oxide aerogel for the adsorption of copper ions*. Nanoscience and Nanotechnology Letters, 2014. **6**(11): p. 1018-1023.
15. Kim, S.R., M.K. Parvez, and M. Chhowalla, *UV-reduction of graphene oxide and its application as an interfacial layer to reduce the back-transport reactions in dye-sensitized solar cells*. Chemical Physics Letters, 2009. **483**(1): p. 124-127.
16. Sabbatini, P., et al., *Fabrication and characterization of iron oxide ceramic membranes for arsenic removal*. Water research, 2010. **44**(19): p. 5702-5712.
17. Hofs, B., et al., *Comparison of ceramic and polymeric membrane permeability and fouling using surface water*. Separation and Purification Technology, 2011. **79**(3): p. 365-374.
18. Mueller, U., G. Biwer, and G. Baldauf, *Ceramic membranes for water treatment*. Water Science and Technology: Water Supply, 2010. **10**(6): p. 987-994.
19. Mueller, U. and M. Witte, *Ceramic membranes—Case related protocol for optimal operational conditions to treat filter backwash water*. DWTC (TZW), Techneau, 2007.

20. Lu, D., et al., *Influence of surface properties of filtration-layer metal oxide on ceramic membrane fouling during ultrafiltration of oil/water emulsion*. Environmental science & technology, 2016. **50**(9): p. 4668-4674.
21. Sabbatini, P., et al., *Fabrication and characterization of iron oxide ceramic membranes for arsenic removal*. Water Research, 2010. **44**(19): p. 5702-5712.
22. Sentana, I., et al., *Reduction of chlorination byproducts in surface water using ceramic nanofiltration membranes*. Desalination, 2011. **277**(1-3): p. 147-155.
23. Liu, L., et al., *Concurrent filtration and solar photocatalytic disinfection/degradation using high-performance Ag/TiO₂ nanofiber membrane*. Water Research, 2012. **46**(4): p. 1101-1112.
24. Storms, M.I., *Surface interactions between nanoscale iron and organic material: potential uses in water treatment process units*. 2015, University of Missouri--Columbia.
25. Zabarskas, V., et al., *Analysis of Fe₃O₄ protective coatings thermally grown on color picture TV tube structural steel components*. Mater Sci-Medzg, 2004. **10**(2): p. 147-151.
26. Schwertmann, U. and R. Cornell, *The Iron Oxides-Structure, Properties, Reactions, Occurrence and Uses*. 1996, New York: VCH.
27. Schwertmann, U. and R.M. Cornell, *Iron Oxides in the Laboratory. Preparation and Characterisation*. 1991, New York: VCH.
28. Yao, P., K.H. Choo, and M.H. Kim, *A hybridized photocatalysis-microfiltration system with iron oxide-coated membranes for the removal of natural organic matter in water treatment: Effects of iron oxide layers and colloids*. Water Research, 2009. **43**(17): p. 4238-4248.
29. Davies, S.H., et al., *Fabrication of catalytic ceramic membranes for water filtration*, in *Water Science and Technology: Water Supply*. 2010. p. 81-86.
30. Harman, B.I., et al., *The use of iron oxide-coated ceramic membranes in removing natural organic matter and phenol from waters*. Desalination, 2010. **261**(1-2): p. 27-33.
31. Hackley, V.A. and M.A. Anderson, *Synthesis and characterization of unsupported ferric oxide ceramic membranes*. Journal of Membrane Science, 1992. **70**(1): p. 41-51.
32. Sawyer, C.N., P.L. McCarty, and G.F. Perkin, *Chemistry for Environmental Engineering*. 1994, New York: McGraw-Hill.
33. J. Rose, M.C.-F., S. Moustier, C. Magnetto, C. Jones, A. Barron, M. Wiesner, J.-Y. Bottero, *Synthesis and characterization of carboxylate-FeOOH nanoparticles (ferroxanes) and ferroxane-derived ceramics*. Chemistry of Materials, 2002. **14**: p. 621-628.
34. Cortalezzi, M.a.M., et al., *Ceramic membranes derived from ferroxane nanoparticles: a new route for the fabrication of iron oxide ultrafiltration membranes*. Journal of Membrane Science, 2003. **227**(1-2): p. 207-217.
35. Fidalgo de Cortalezzi, M.M., et al., *Virus removal by iron oxide ceramic membranes*. Journal of Environmental Chemical Engineering, 2014. **2**(3): p. 1831-1840.
36. Hou, W.-C., et al., *Photochemical transformation of graphene oxide in sunlight*. Environmental science & technology, 2015. **49**(6): p. 3435-3443.
37. Li, J., et al., *Removal of Cu (II) and fulvic acid by graphene oxide nanosheets decorated with Fe₃O₄ nanoparticles*. ACS applied materials & interfaces, 2012. **4**(9): p. 4991-5000.
38. Ji, L., et al., *Graphene nanosheets and graphite oxide as promising adsorbents for removal of organic contaminants from aqueous solution*. Journal of environmental quality, 2013. **42**(1): p. 191-198.

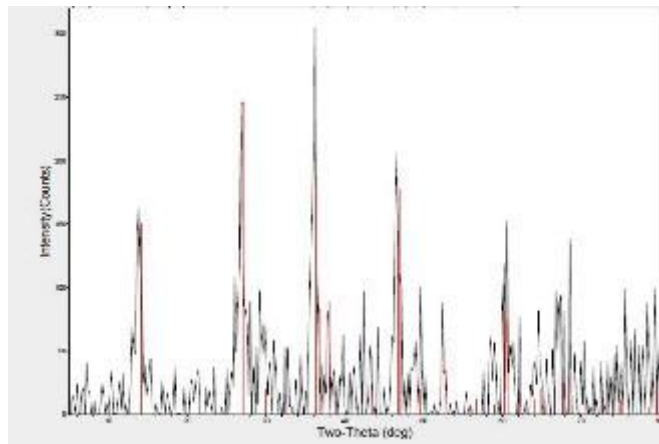
39. Seabra, A.B., et al., *Nanotoxicity of graphene and graphene oxide*. Chemical research in toxicology, 2014. **27**(2): p. 159-168.
40. Jastrzębska, A.M. and A.R. Olszyna, *The ecotoxicity of graphene family materials: current status, knowledge gaps and future needs*. Journal of Nanoparticle Research, 2015. **17**(1): p. 1-21.
41. Frankenberger Jr, W.T., *Environmental chemistry of arsenic*. 2001: CRC Press.
42. Robertson, F.N., *Arsenic in ground-water under oxidizing conditions, south-west United States*. Environmental geochemistry and Health, 1989. **11**(3-4): p. 171-185.
43. Smedley, P.L., *Sources and distribution of arsenic in groundwater and aquifers*. 2008.
44. Jeong, Y., *The adsorption of arsenic (V) by iron (Fe₂O₃) and aluminum (Al₂O₃) oxides*. 2005.
45. Fleischer, M., *Glossary of mineral species: Tucson, Ariz., Mineralogical Record*. 1983, Inc.
46. Kim, M.-J., J. Nriagu, and S. Haack, *Arsenic species and chemistry in groundwater of southeast Michigan*. Environmental Pollution, 2002. **120**(2): p. 379-390.
47. Hinkle, S.R. and D.J. Polette, *Arsenic in ground water of the Willamette Basin, Oregon*. 1999, US Dept. of the Interior, US Geological Survey.
48. Smith, A.H., et al., *Arsenic epidemiology and drinking water standards*. Science, 2002. **296**(5576): p. 2145-2146.
49. Chen, Y. and H. Ahsan, *Cancer burden from arsenic in drinking water in Bangladesh*. American Journal of Public Health, 2004. **94**(5): p. 741-744.
50. Roy, P. and A. Saha, *Metabolism and toxicity of arsenic: A human carcinogen*. Current Science, 2002. **82**(1): p. 38-45.
51. Abernathy, C.O., R.L. Calderon, and W.R. Chappell, *Arsenic: exposure and health effects*. 2012: Springer Science & Business Media.
52. Johnston, R. and H. Heijnen, *Safe water technology for arsenic removal*. Technologies for arsenic removal from drinking water, 2001: p. 1-22.
53. Ghurye, G., D. Clifford, and A. Tripp, *Iron coagulation and direct microfiltration to remove arsenic from groundwater*. Journal (American Water Works Association), 2004. **96**(4): p. 143-152.
54. Brandhuber, P. and G. Amy, *Alternative methods for membrane filtration of arsenic from drinking water*. Desalination, 1998. **117**(1): p. 1-10.
55. Worch, E., *Adsorption technology in water treatment: fundamentals, processes, and modeling*. 2012: Walter de Gruyter.
56. Ali, I. and V. Gupta, *Advances in water treatment by adsorption technology*. Nature protocols, 2006. **1**(6): p. 2661-2667.
57. WEBER JR, W.J. *The University of Michigan, College of Engineering, Ann Arbor, Michigan 48104, USA*. in *XXIVth International Congress of Pure and Applied Chemistry: Main Section Lectures Presented at Two Joint Symposia Held During the Above Congress at Hamburg, Federal Republic of Germany, 2-8 September 1973*. 2013. Butterworth-Heinemann.
58. Rose, J., et al., *Synthesis and characterization of carboxylate-FeOOH nanoparticles (ferroxanes) and ferroxane-derived ceramics*. Chemistry of Materials, 2002. **14**(2): p. 621-628.
59. Chen, J., et al., *An improved Hummers method for eco-friendly synthesis of graphene oxide*. Carbon, 2013. **64**: p. 225-229.

60. Cornell, R.M. and U. Schwertmann, *The iron oxides: structure, properties, reactions, occurrences and uses*. 2003: John Wiley & Sons.
61. Zhao, J., et al., *Heteroaggregation of graphene oxide with minerals in aqueous phase*. *Environmental science & technology*, 2015. **49**(5): p. 2849-2857.
62. Barbara, L.D., *Louisiana State University, Christine M. Clark*, Eastern Michigan University. X-ray Powder Diffraction (XRD) Geochemical Instrumentation and Analysis.
63. Cullity, B.D., *Elements of X-Ray Diffraction, 2nd Edition*. 1978, Reading, Massachusetts: Addison-Wesley Publishing Company.
64. Instruments, M., *Zetasizer nano series user manual*. MAN0317, 2004(1.1).
65. Hunter, R.J., *Zeta potential in colloid science: principles and applications*. Vol. 2. 2013: Academic press.
66. Brunauer, S., P.H. Emmett, and E. Teller, *Adsorption of gases in multimolecular layers*. *Journal of the American chemical society*, 1938. **60**(2): p. 309-319.
67. Berg, J., *An Introduction to Interfaces & Colloids: The Bridge to Nanoscience*. 2010, Hackensack, NJ: World Scientific Publishing Co.
68. Bindell, J., *Scanning Electron Microscopy*. *Encyclopedia of Materials Characterization: Surfaces, Interfaces, Thin Films*, ed. R. Brundle and C. Evans. 1992, Greenwich: Manning Publication Company.
69. Foo, K. and B. Hameed, *Insights into the modeling of adsorption isotherm systems*. *Chemical Engineering Journal*, 2010. **156**(1): p. 2-10.
70. Ne, N., *Atomic absorption spectrometry*.
71. García, R. and A. Báez, *Atomic Absorption Spectrometry (AAS)*. *Atomic Absorption Spectroscopy*, 2012. **1**: p. 1-13.
72. Lagergren, S., *Zur theorie der sogenannten adsorption gelöster stoffe*. 1898: PA Norstedt & söner.
73. Saha, B. and C. Orvig, *Biosorbents for hexavalent chromium elimination from industrial and municipal effluents*. *Coordination Chemistry Reviews*, 2010. **254**(23): p. 2959-2972.
74. Yuh-Shan, H., *Citation review of Lagergren kinetic rate equation on adsorption reactions*. *Scientometrics*, 2004. **59**(1): p. 171-177.
75. Ho, Y.-S. and G. McKay, *Pseudo-second order model for sorption processes*. *Process biochemistry*, 1999. **34**(5): p. 451-465.
76. Tammann, G. and W. Köster, *Metallographische Mitteilungen aus dem Institut für physikalische Chemie der Universität Göttingen. CV. Die Geschwindigkeit der Einwirkung von Sauerstoff, Schwefelwasserstoff und Halogenen auf Metalle*. *Zeitschrift für anorganische und allgemeine Chemie*, 1922. **123**(1): p. 196-224.
77. Aharoni, C. and F. Tompkins, *Kinetics of adsorption and desorption and the Elovich equation*. *Advances in Catalysis*, 1970. **21**: p. 1-49.
78. Wu, F.-C., R.-L. Tseng, and R.-S. Juang, *Characteristics of Elovich equation used for the analysis of adsorption kinetics in dye-chitosan systems*. *Chemical Engineering Journal*, 2009. **150**(2): p. 366-373.
79. Freundlich, H., *Über die adsorption in lösungen [Adsorption in solution]*” *Zeitschrift für Physikalische Chemie*, 57. 1906.
80. Temkin, M. and V. Pyzhev, *Kinetics of ammonia synthesis on promoted iron catalysts*. *Acta physiochim. URSS*, 1940. **12**(3): p. 217-222.

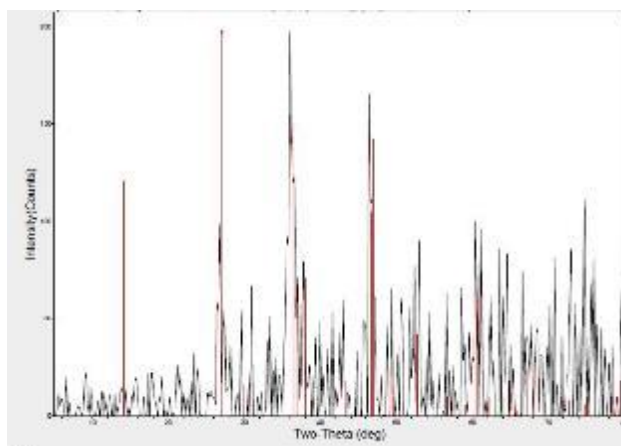
81. Li, M.-j., et al., *The evolution of surface charge on graphene oxide during the reduction and its application in electroanalysis*. Carbon, 2014. **66**: p. 302-311.
82. Lee, C., et al., *Measurement of the elastic properties and intrinsic strength of monolayer graphene*. science, 2008. **321**(5887): p. 385-388.
83. Dreyer, D.R., et al., *The chemistry of graphene oxide*. Chemical Society Reviews, 2010. **39**(1): p. 228-240.
84. Wang, Z.-l., et al., *Facile, mild and fast thermal-decomposition reduction of graphene oxide in air and its application in high-performance lithium batteries*. chemical communications, 2012. **48**(7): p. 976-978.
85. Shih, C.-J., et al., *Understanding the pH-dependent behavior of graphene oxide aqueous solutions: a comparative experimental and molecular dynamics simulation study*. Langmuir, 2011. **28**(1): p. 235-241.
86. Amy, G.L., et al., *Adsorbent treatment technologies for arsenic removal*. 2005: American Water Works Association.
87. Jia, Y., et al., *Infrared spectroscopic and X-ray diffraction characterization of the nature of adsorbed arsenate on ferrihydrite*. Geochimica et Cosmochimica Acta, 2007. **71**(7): p. 1643-1654.
88. Zhao, K. and H. Guo, *Behavior and mechanism of arsenate adsorption on activated natural siderite: evidences from FTIR and XANES analysis*. Environmental Science and Pollution Research, 2014. **21**(3): p. 1944-1953.
89. Vuong Hoan, N.T., et al., *Fe₃O₄/Reduced Graphene Oxide Nanocomposite: Synthesis and Its Application for Toxic Metal Ion Removal*. Journal of Chemistry, 2016. **2016**.
90. Wan, S., et al., *Rapid and highly selective removal of lead from water using graphene oxide-hydrated manganese oxide nanocomposites*. Journal of hazardous materials, 2016. **314**: p. 32-40.
91. Cumbal, L. and A.K. SenGupta, *Arsenic removal using polymer-supported hydrated iron (III) oxide nanoparticles: role of Donnan membrane effect*. Environmental science & technology, 2005. **39**(17): p. 6508-6515.
92. Mamindy-Pajany, Y., et al., *Arsenic adsorption onto hematite and goethite*. Comptes Rendus Chimie, 2009. **12**(8): p. 876-881.

9 Appendix

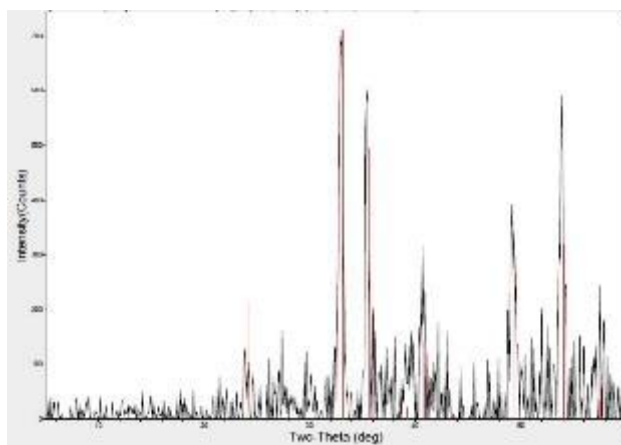
Appendix A



(1) XRD diffractogram for lepidocrocite



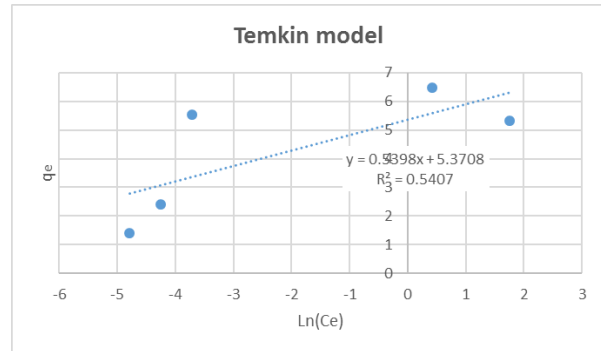
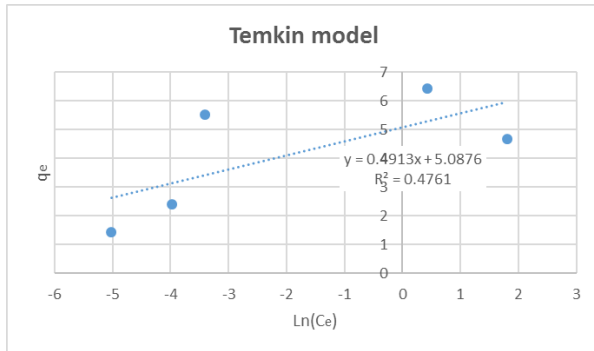
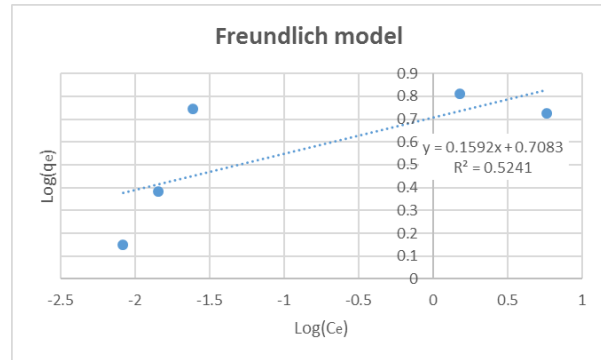
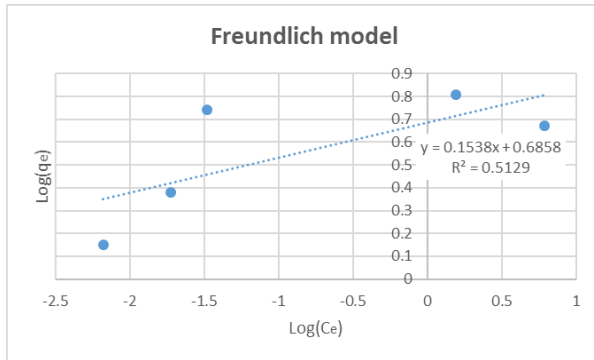
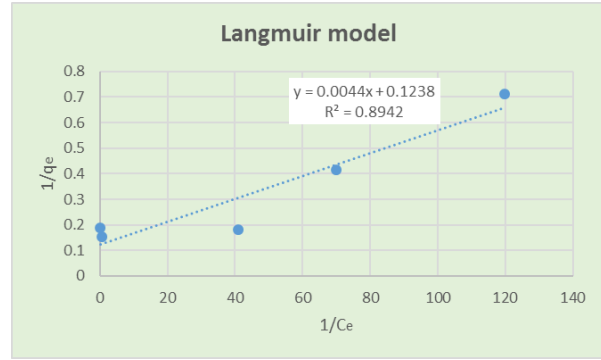
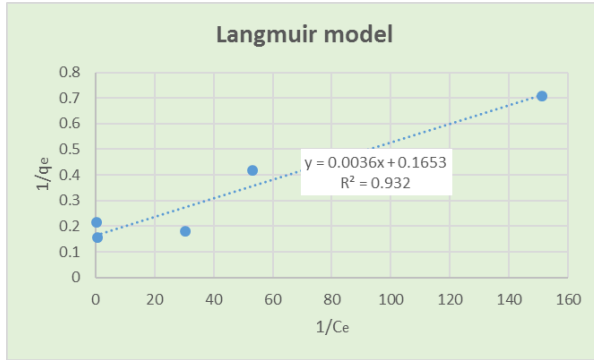
(2) XRD diffractogram for ferroxane nanoparticles



(3) XRD diffractogram for hematite

Appendix B

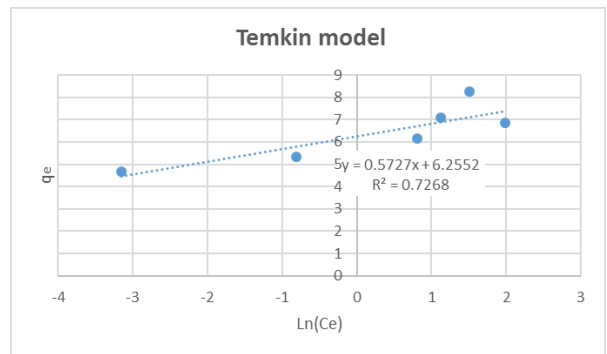
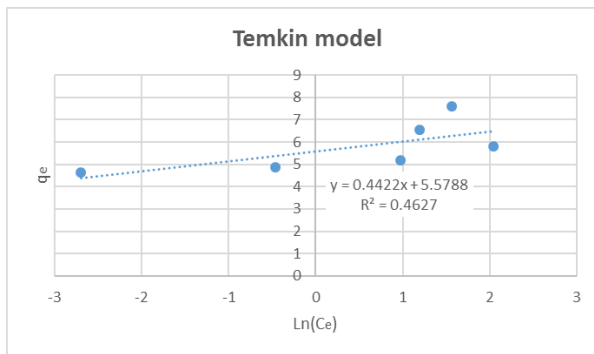
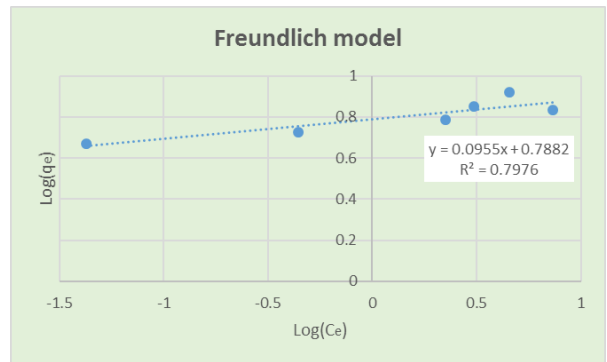
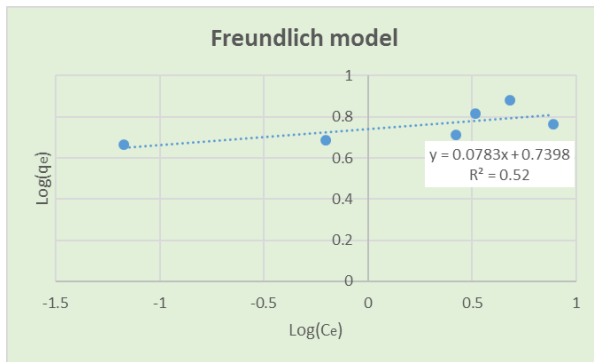
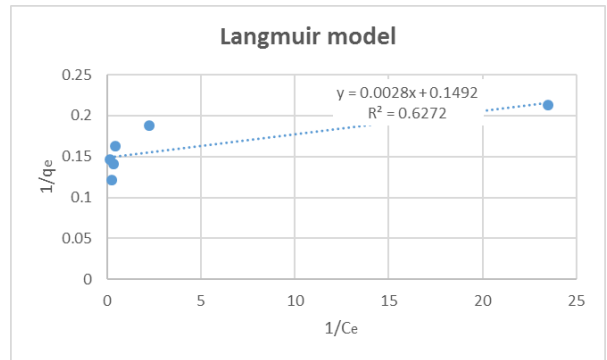
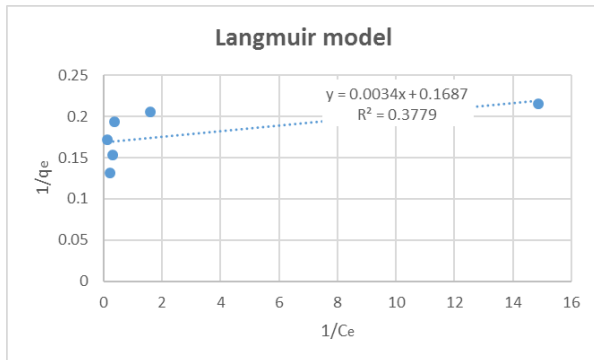
B-1: Linear fitting for the three models when the adsorption condition is pH 4.5 and I.S. 1 mM



(a) 5% GO/IO

(b) 10% GO/IO

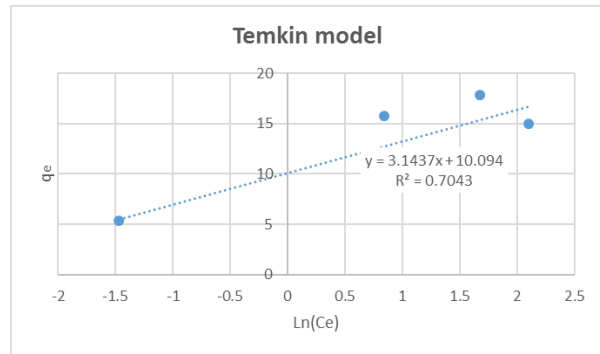
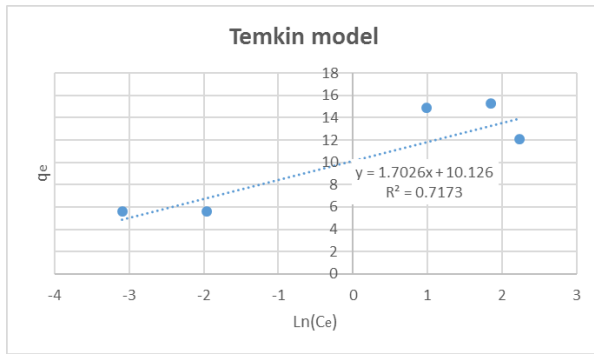
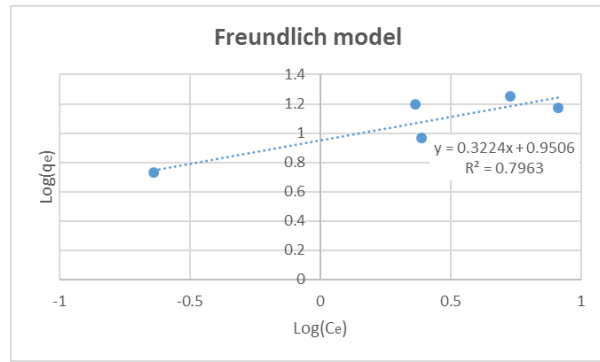
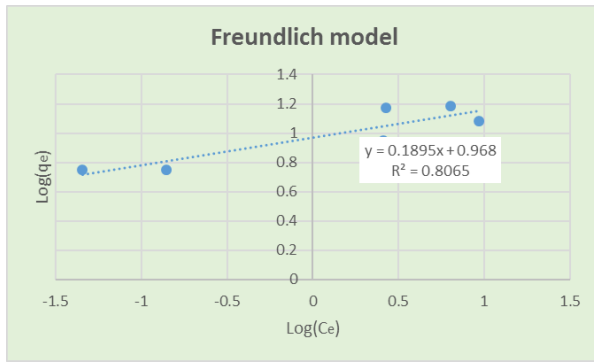
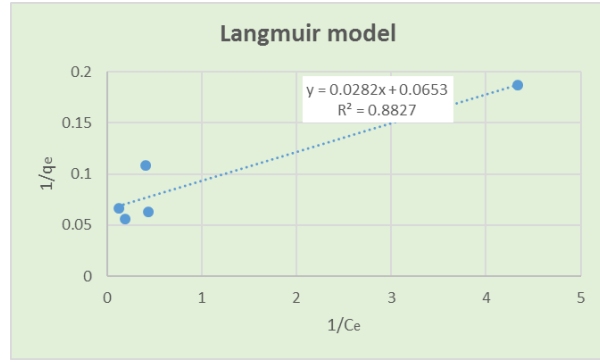
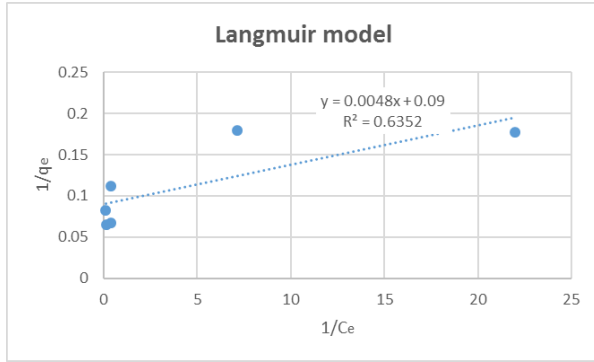
B-2: Linear fitting for the three models when the adsorption condition is pH 7 and I.S. 1 mM



(a) 5% GO/IO

(b) 10% GO/IO

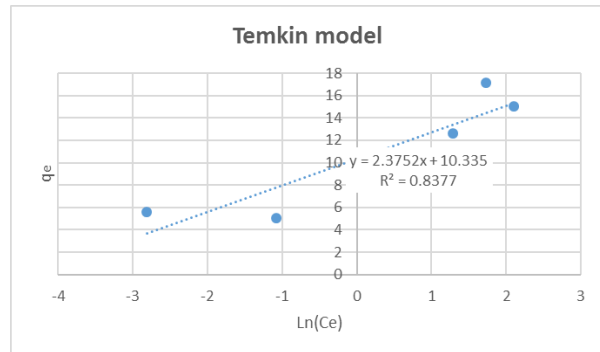
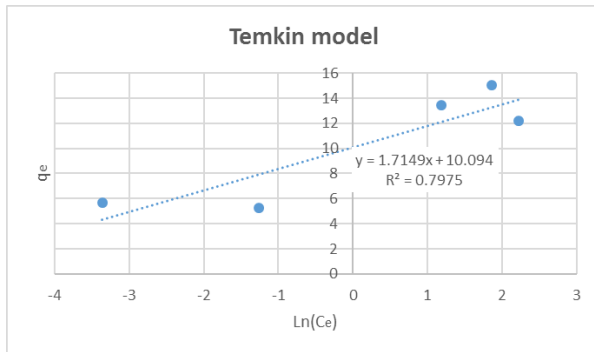
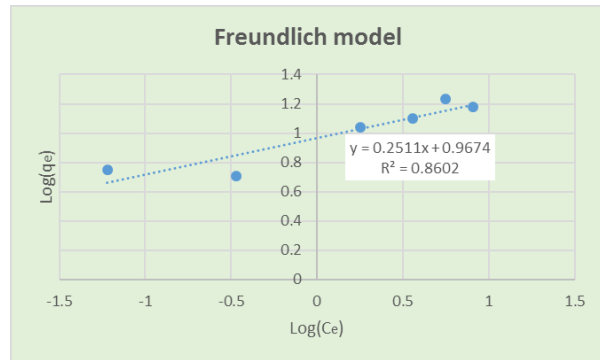
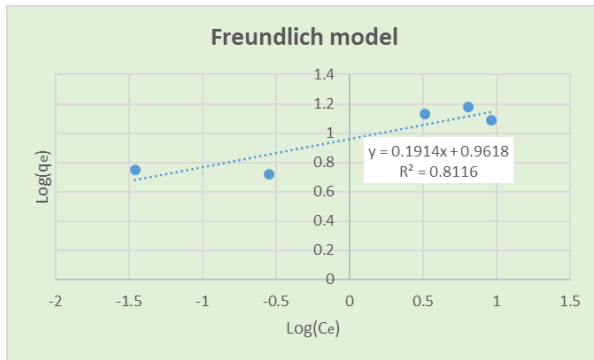
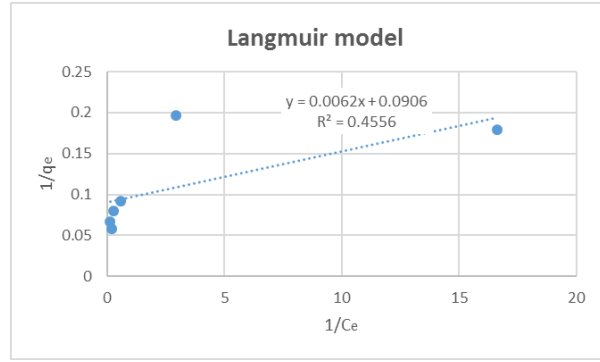
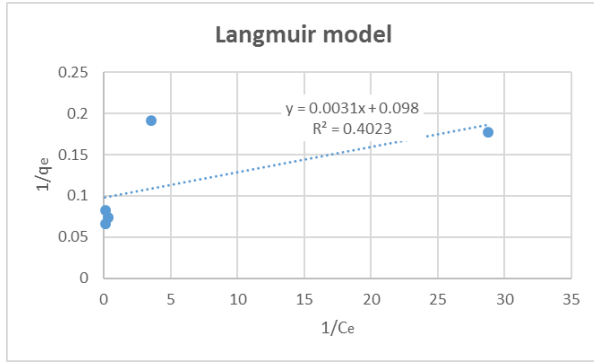
B-3: Linear fitting for the three models when the adsorption condition is pH 4.5 and I.S. 100 mM



(a) 5% GO/IO

(b) 10% GO/IO

B-4: Linear fitting for the three models when the adsorption condition is pH 7 and I.S. 100 mM

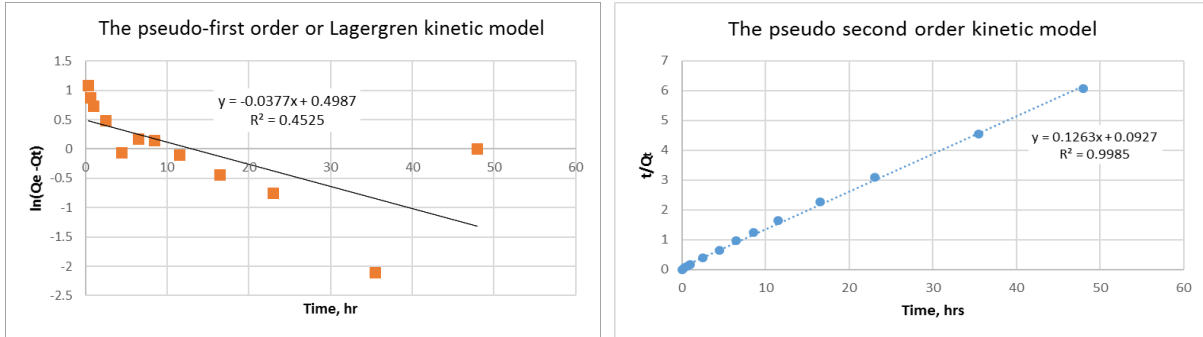


(a) 5% GO/IO

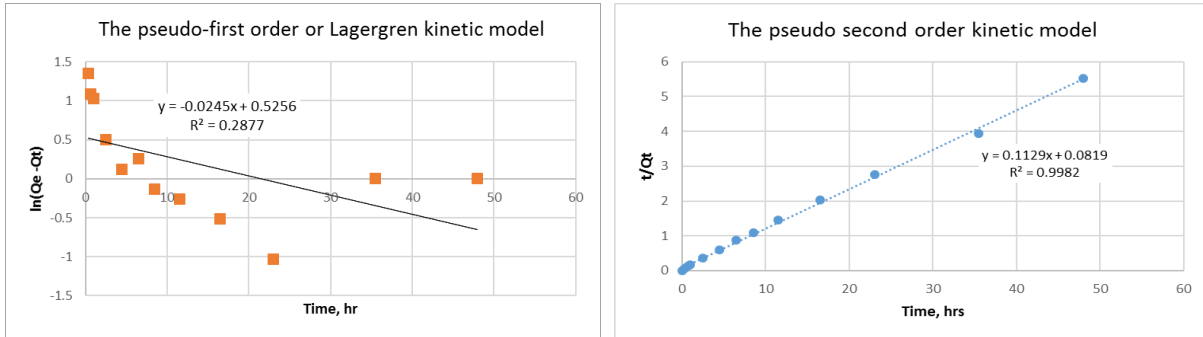
(b) 10% GO/IO

Appendix C

Linear methods of kinetics models and experimental kinetics for arsenic adsorption by (a) 5% and (b) 10% composite materials.



(a)



(b)